SANDIA REPORT

SAND99–0189
Unlimited Release
Printed February 1999

Explosive Containment Chamber Vulnerability to Chemical Munition Fragment Impact

M. E. Kipp, R. R. Martinez, R. A. Benham, and S. H. Fischer

Prepared by
Sandia National Laboratories
Albuquerque, New Mexico 87185 and Livermore, California 94550

Sandia is a multiprogram laboratory operated by Sandia Corporation, a Lockheed Martin Company, for the United States Department of Energy under Contract DE-AC04-94AL85000.

Sandia National Laboratories

Issued by Sandia National Laboratories, operated for the United States Department of Energy by Sandia Corporation.

Available to DOE and DOE contractors from
Office of Scientific and Technical Information
P.O. Box 62
Oak Ridge, TN 37831

Prices available from (703) 605-6000
Web site: http://www.ntis.gov/ordering.htm

Available to the public from
National Technical Information Service
U.S. Department of Commerce
5285 Port Royal Rd
Springfield, VA 22161

NTIS price codes
Printed copy: A03
Microfiche copy: A01

SAND99 - 0189
Unlimited Distribution
Printed February 1999

Explosive Containment Chamber Vulnerability to Chemical Munition Fragment Impact

M. E. Kipp and R. R. Martinez
Computational Physics Department
and
R. A. Benham and S. H. Fischer
Explosive Components Department

Sandia National Laboratories
P.O. Box 5800
Albuquerque, NM 87185-0820

ABSTRACT

Scenarios in which the explosive burster charge in a chemical munition accidentally detonates inside demilitarization containment chambers are analyzed. The vulnerability of an inner Auxiliary Pressure Vessel and the primary Explosive Containment Chamber to impact by fragments from the largest explosive charge expected to be placed in these chambers (M426, 8 inch, chemical, 7 lbs Comp B) is evaluated. Numerical (CTH) and empirical (ConWep) codes are used to characterize the munition fragments, and assess the consequences of their impact and penetration on the walls of these vessels. Both pristine and corroded configurations of the munition have been considered, with and without liquid agent fill. When the munition burster charge detonates, munition case fragments impact and perforate the Auxiliary Pressure Vessel wall, resulting in extensive breakup of this inner chamber and the formation of additional fragments. These residual munition case and Auxiliary Pressure Vessel fragments have sufficient mass and velocity to crater the Explosive Containment Chamber inner wall layer, with accompanying localized permanent deformation (bulging) of both the inner and outer chamber walls. The integrity of the Explosive Containment Chamber was retained under all of the APV / munition configurations considered in this study, with no evidence that primary (munition) or secondary (munition and Auxiliary Pressure Vessel) fragments will perforate the inner chamber wall. Limited analyses of munition detonation without the Auxiliary Pressure Vessel present indicate that some munition spall fragments could form under those conditions that have sufficient mass and velocity to perforate the inner wall of the Explosive Containment Chamber.

EXECUTIVE SUMMARY

Scenarios in which the explosive burster charge in a chemical munition accidentally detonates inside demilitarization containment chambers are analyzed. The vulnerability of an inner Auxiliary Pressure Vessel (APV) and the primary Explosive Containment Chamber (ECC) to impact by fragments from the largest explosive charge expected to be placed in these chambers (M426, 8 inch, chemical, 7 lbs Comp B) is evaluated. Numerical (CTH) and empirical (ConWep) codes are used to characterize the munition fragments, and assess the consequences of their impact and penetration on the walls of these vessels. Both pristine and corroded configurations of the munition have been considered, with and without liquid agent fill. When the munition burster charge detonates, munition case fragments impact and perforate the Auxiliary Pressure Vessel wall, resulting in extensive breakup of this inner chamber. The impact leads to decreased velocity and further breakup of the munition case fragments, and the formation of additional fragments from the APV wall. These residual munition case and Auxiliary Pressure Vessel fragments have sufficient mass and velocity to crater the Explosive Containment Chamber inner wall, with accompanying localized permanent deformation (bulging) of both the inner and outer chamber walls. The integrity of the Explosive Containment Chamber was retained under all of the APV / munition configurations considered in this study, with no evidence that primary (munition) or secondary (munition and Auxiliary Pressure Vessel) fragments will perforate the inner chamber wall.

Munition case fragment characteristic dimensions were determined from the strain rate conditions at the time of fracture. Random scoring of the munition case was used to effect statistical breakup of the case, and analyze the interaction of these fragments with the APV wall. The post-impact results were used to characterize the dimensions and velocities of the most lethal fragments expected to impact the ECC inner wall. Maximum velocities of about 400 m/s and masses of about 1200 g were obtained. Impacts of fragments onto the ECC wall structure were numerically calculated with the CTH shock physics code, for both three dimensional fragments and two dimensional equivalent rods. Significant cratering at the impacted surface and permanent deformation of both the inner and outer walls occurs. This munition and chamber assembly was also modeled with the ConWep code. The maximum depths of penetration ranged from one-third to two-thirds of the inner ECC wall, depending on the method of analysis. The effects of varying the burster charge initiation location, exclusion of agent, and corrosion of the munition case (idealized as one-half thickness) on the fragment characteristics were evaluated. These analyses confirmed that the most lethal fragments had been utilized in the assessment of ECC integrity for this chemical munition accident scenario.

The presence of the Auxiliary Pressure Vessel is a very important intervening structure between the munition and Explosive Containment Chamber. Limited analyses of munition detonation without the Auxiliary Pressure Vessel present indicate that some munition spall fragments form that have sufficient mass and velocity to perforate the inner wall of the Explosive Containment Chamber. It was determined that if the munition is drained of agent, the impact of the burster shells on the inside of the munition case spall thin layers of case material off the exterior of the munition at velocities of about 1000 m/s. The resulting fragments are capable of perforating the inner 30 mm wall of the Explosive Containment Chamber.

Acknowledgments

The authors gratefully acknowledge K. L. Tschritter for support provided during the course of this study, D. Childers (Teledyne-Brown, Huntsville) for insights into the geometry for the major components, and E. Rudicille (ARL, Aberdeen) for material property information and the detailed description of the M426 munition. W. Taylor, J. Hawks, and R. DiBerido, U. S. Army, Aberdeen, also provided helpful comments during reviews of these analyses.

CONTENTS Page

I. INTRODUCTION

Demilitarization of chemical agent munitions containing explosive burster charges is proposed to be undertaken in closed chambers to fully contain all the agent. In a current design, the munition is loaded into an Auxiliary Pressure Vessel (APV), which is then inserted into an Explosion Containment Chamber (ECC), both of which are sealed containment vessels. The APV has externally mounted equipment designed to drill holes into the munition secured within in preparation for extracting the chemical agent and cleaning the munition for subsequent removal of the explosive charge and disposal, all designed to be accomplished without leaking contaminants. The breaching and cleansing operations are done within the ECC to preclude the dispersal of any chemical agent in case of accidental detonation of the munition charge. The ECC has been designed to sustain detonation of an explosive mass that is significantly larger than any expected charge mass in the inventory to be demilitarized.

The detonation of a munition burster charge, however, will not only generate a blast wave, it will be accompanied by fragments formed from both the munition case and the inner containment vessel (APV). The purpose of this report is to evaluate the potential damage to the Explosion Containment Chamber from the fragments that would form in the event of accidental detonation of a munition with the largest mass of burster explosive (i.e., a worst case scenario). To this end, the munition chosen as representing such a severe accident condition was the M426, an 8-inch chemical round containing 7 lbs of explosive and about 15 lbs of chemical agent. Two possible conditions under which an accidental detonation could occur were considered. Drilling operations to breach the munition case are located near the center of the munition, so central initiation of the charge would be indicated, although limit devices are expected to preclude entry into the explosive charge. Initiation of the charge by a faulty fuze, perhaps activated by the drilling operation, or other vibration, was also considered a reasonable possibility. Recovered munitions from burial sites might be found in corroded conditions, and some analyses were made presuming significant case material loss, and possible chemical agent absence. For the primary analyses, the munition was presumed to be located within the APV when it detonated; a few cases were considered without the APV. The blast effects of the explosion on the ECC were not addressed in this study.

The analyses focused on the fragment formation from the detonating munition, and the vulnerability of the ECC to fragment impact. Two approaches to the fragment analyses were taken: (1) explicit modeling of the exploding munition in the APV, determination of the resulting fragment dimensions, and fragment impact onto the ECC, and (2) use of an empirical code that utilizes conventional weapon fragment databases to determine the fragment formation and target response.

For explicit modeling of detonation and fragment impact, the numerical simulations were made with the CTH Eulerian shock wave propagation code (McGlaun, *et al.*,1990). This multi-dimensional shock physics Eulerian code, developed and maintained at Sandia National Laboratories, has the capability to model dynamic events that include explosive detonation and high velocity impact. The CTH code solves the differential equations describing conservation of mass, momentum and energy during transient dynamic events on a fixed spatial mesh. CTH is a multi-dimensional code capable of tracking the interactions of up to 20 materials. This code contains models suitable to describe material response under most conditions encountered in shock

physics, including the inert solids and explosives for the current application. A variety of insert geometries facilitate the analyses of complex devices. The Eulerian structure of the code permits large deformations associated with explosive or impact events to be accommodated. The primary means of obtaining characteristic fragment dimensions in the numerical simulations is to determine the strain rate at the time of fracture from a detailed analysis of the material motion. Appendix A describes the basic relationships between the strain rate and the fragment dimensions that result as materials fracture under high strain rate loading conditions. In the numerical simulations, CTH accommodates fracture by injecting void into a cell to effect the unloading from a tensile state to a state of zero stress. As a consequence, when interface plots are made using 50% volume fraction as the boundary measure, the calculation has the appearance of having broken the material into discrete fragments. Although the material is indeed dispersed, the actual fragment size is more accurately taken from the analytical forms in Appendix A.

An alternate approach to determining the fragment formation from an exploding munition is to use the ConWep conventional weapons effects code (ConWep, 1989). ConWep uses Gurney calculations for calculating the approximate speeds of fragments driven by high explosives (Kennedy, 1970; Jones, et al., 1980). Formulas are available for a variety of simple configurations in which the explosive is in contact with the solid materials that form the fragments. The fragment sizes and velocities determined by ConWep, based on empirical data, are then used to evaluate the penetration into targets, again utilizing empirical data.

An accurate determination of what would be considered a worst case fragment from the munition detonation presented the most difficulties in this study. The incident velocities of the case fragments can be fairly well bounded for the burster explosive employed in this munition, including the velocity changes after interaction of these fragments with the APV - both the CTH code calculations and ConWep give similar amplitudes for the source velocities. There were no arena test data available to guide the fragment dimensions, so strong reliance on analytic measures and related empirical data was required. Choosing an unrealistically large fragment to be "conservative" may lead to an overestimation of the protection demanded, but an equally serious error would be to underestimate the maximum fragment size that could form.

In the following sections, the containment vessels and munition configurations are defined (Section II), and an accident scenario is examined in detail (Section III). In this latter section, the focus is on characterizing the possible fragments from the munition detonation in the Auxiliary Pressure Vessel, then evaluating consequences of fragment impacts on the Explosion Containment Chamber wall structure. Appendices have been included that summarize the fragmentation model (Appendix A), the material parameters used in the CTH code calculations (Appendix B), and a comparison of limit velocity data with code results to provide the basis for the level of confidence placed in the code simulations that represent the fragment penetration events described in this report (Appendix C). The effect of numerical resolution on the results is discussed in Appendix D. Although analysis of a primary initial configuration of the exploding munition in the Auxiliary Pressure Vessel is the focus of the main body of the report (Section III), many additional numerical simulations were made in support of this primary configuration, and these variations in initial munition configuration and burster explosive initiation point are described in Appendix E.

II. GEOMETRY

The configurations of the Explosion Containment Chamber (ECC), Auxiliary Pressure Vessel (APV), and M426 chemical munition are described in this section. Conjectured variations of the munition from its pristine state have been included in the analyses. The ECC and APV are very complex devices, with many appendages and internal components. These additions to the basic structures were excluded from the analyses, based upon the reduction of velocity and further breakup of the source fragments that additional mass provides. Hence, no additional contribution to the vulnerability of the containment devices was anticipated. The focus was on determining the fragment characteristics created by the explosive source, and consequences of fragments that had unimpeded paths through the APV to impact the ECC wall as representing the worst case scenario.

A. Explosion Containment Chamber

The Explosion Containment Chamber (ECC) is the primary containment device that must retain its integrity in the event an accidental munition detonation should occur. The proof testing of this structure to specified charge masses has been evaluated elsewhere and is not included in the present study. A drawing of the ECC, as mounted for transport, is shown in Figure 1 (Teledyne Brown Engineering, 1998a). The external diameter of this cylindrical chamber is 2.4 m. The cylindrical walls are constructed with an interior steel layer 30 mm thick, a central 30 mm layer consisting of a water/glycol solution, and an exterior steel wall of thickness 15 mm (inset, Figure 1). The properties of the steel are tabulated in Appendix B.

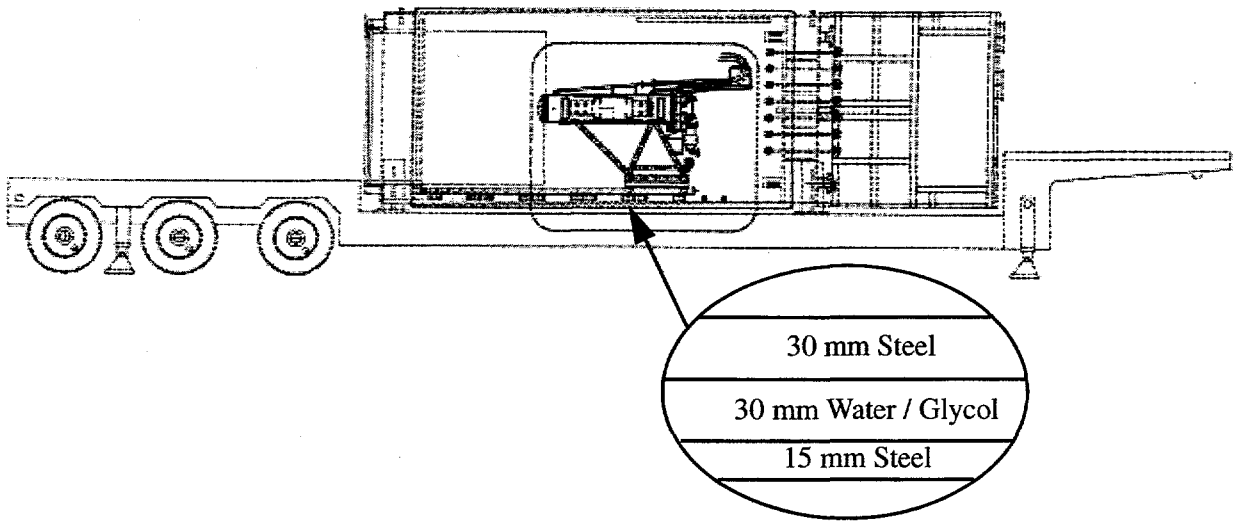

Figure 1. Configuration of the Explosion Containment Chamber on a trailer, with a view of the Auxiliary Pressure Vessel interior to the chamber. Inset shows the layered structure of the cylindrical chamber wall.

B. Auxiliary Pressure Vessel

The Auxiliary Pressure Vessel (APV) is constructed of nominal 12 inch 316L stainless steel pipe, with a 3/8 inch wall thickness (Teledyne Brown Engineering, 1998b). The internal diameter of the pipe is 12 inches (30.48 cm), and the external diameter is 12.75 inches (32.385 cm), with a length of approximately 60 inches. Access doors on one end allow entry and egress, and the other end is sealed with a ported structure (Figure 2). The munition is clamped onto a small carriage, and loaded into the APV so that the nose of the projectile points towards the access doors. The axis of the munition coincides with the axis of the APV, and the axial center of the projectile is located at approximately the axial center of the APV. A large carriage assembly is utilized to support and insert the APV into the Explosion Containment Chamber. Rails for the munition carriage and structural members supporting drilling devices are attached to this unit. The properties of the stainless steel are tabulated in Appendix B.

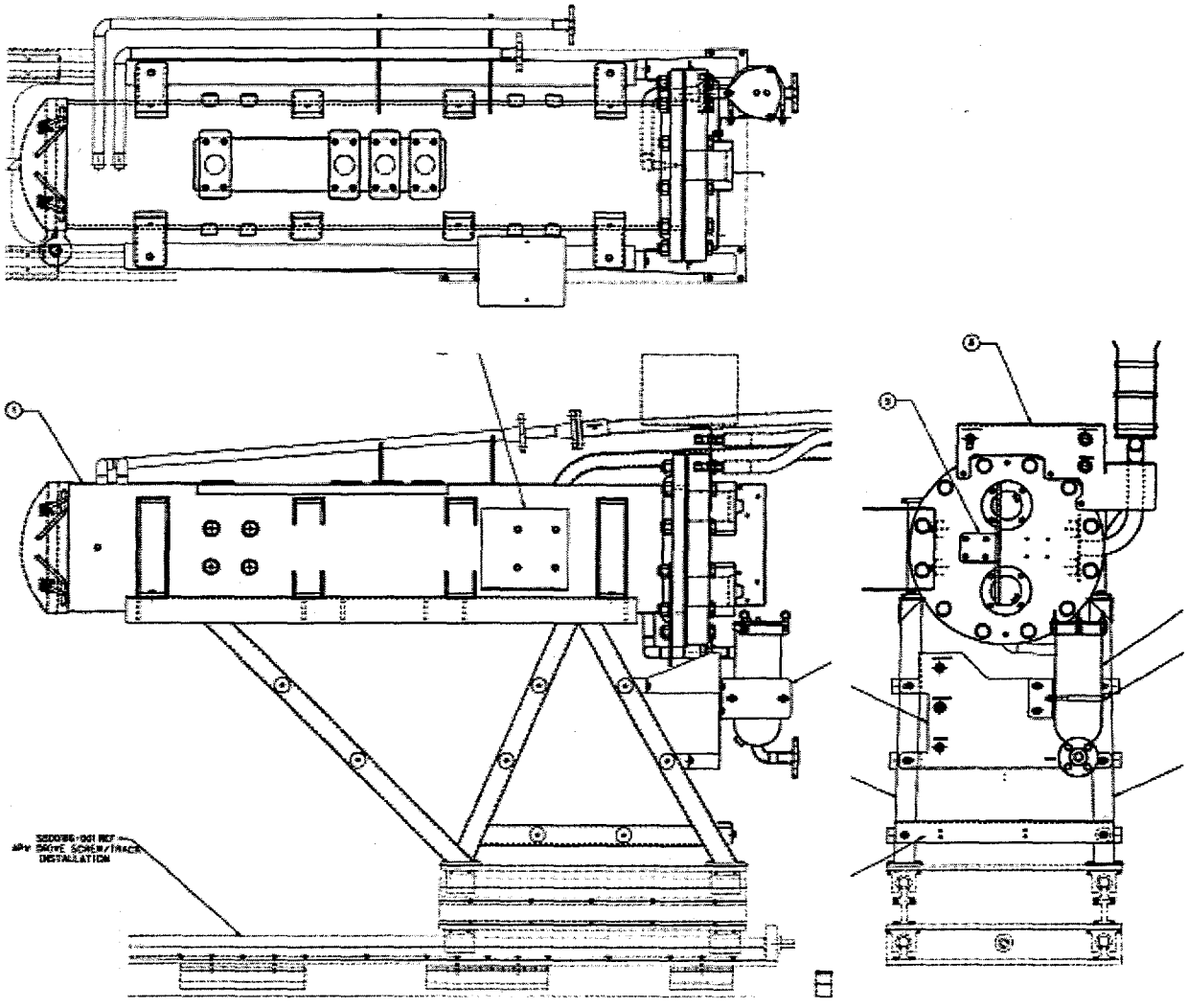

Figure 2. Configuration of the Auxiliary Pressure Vessel.

C. Munition - M426, 8 inch, Chemical

The munition of choice for the current analyses is the M426, 8 inch chemical round, chosen to represent the most severe loading case the Explosion Containment Chamber would be expected to encounter. This projectile contains approximately 7 lb of Comp B explosive for the burster charge, and approximately 15 lb chemical agent. The munition length is about 35 inches, and has a listed total weight of approximately 200 lb. A cross-section view of this projectile is shown in Figure 3 (Picatinny Arsenal, 1962a). The central burster charge extends the full length of the projectile axis, and for normal function, the explosive would be initiated by a forward fuze and booster charge. The explosive is sheathed in a thin aluminum tube. This explosive assembly is located within a thin steel tube, centered in a base cavity, that extends to the shell nose, whose purpose is to isolate the chemical agent in the munition. The thick steel case is capped by a steel nose piece that contains the fuze and a loading ring.

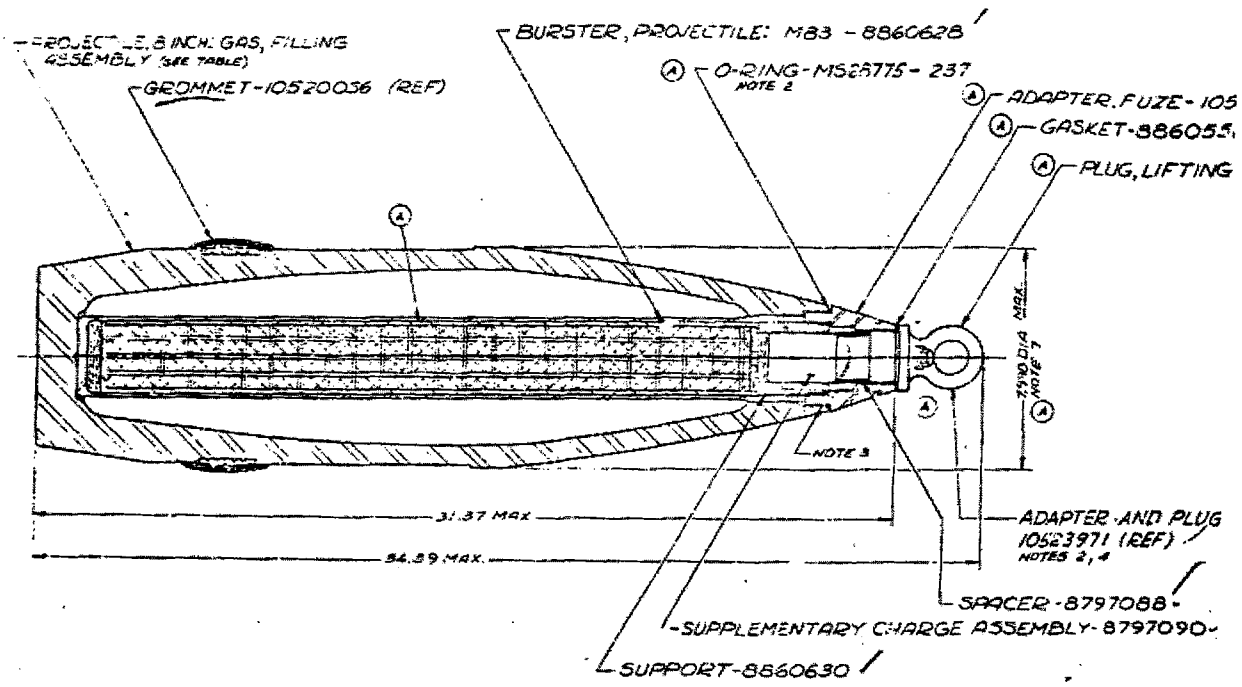

Figure 3. Configuration of the M426 8-inch chemical round.

The numerical model of this munition, constructed to analyze with the CTH Eulerian shock physics code, is a detailed representation of the projectile (Figure 4). The fuze and booster are modeled as a solid piece of aluminum as an approximate description of that region. The chemical agent, with a density of about 0.9 g/cm^3, is modeled as water. The model component masses as defined with the code and actual component masses are compared in Table 1. The largest discrepancy appears in the case mass, where slight variations in modeling the large wall thicknesses contribute to this mass variance; the projectile production total mass may vary as much as 4.5 kg (Picatinny Arsenal, 1962a). The explosive, Comp B, is modeled with standard JWL

parameters (Dobratz and Crawford, 1985). The clamp rings employed to position and stabilize the projectile in the APV are included, as they are rather massive relative to the adjacent munition case thickness. The material parameters for the munition are listed in Appendix B.

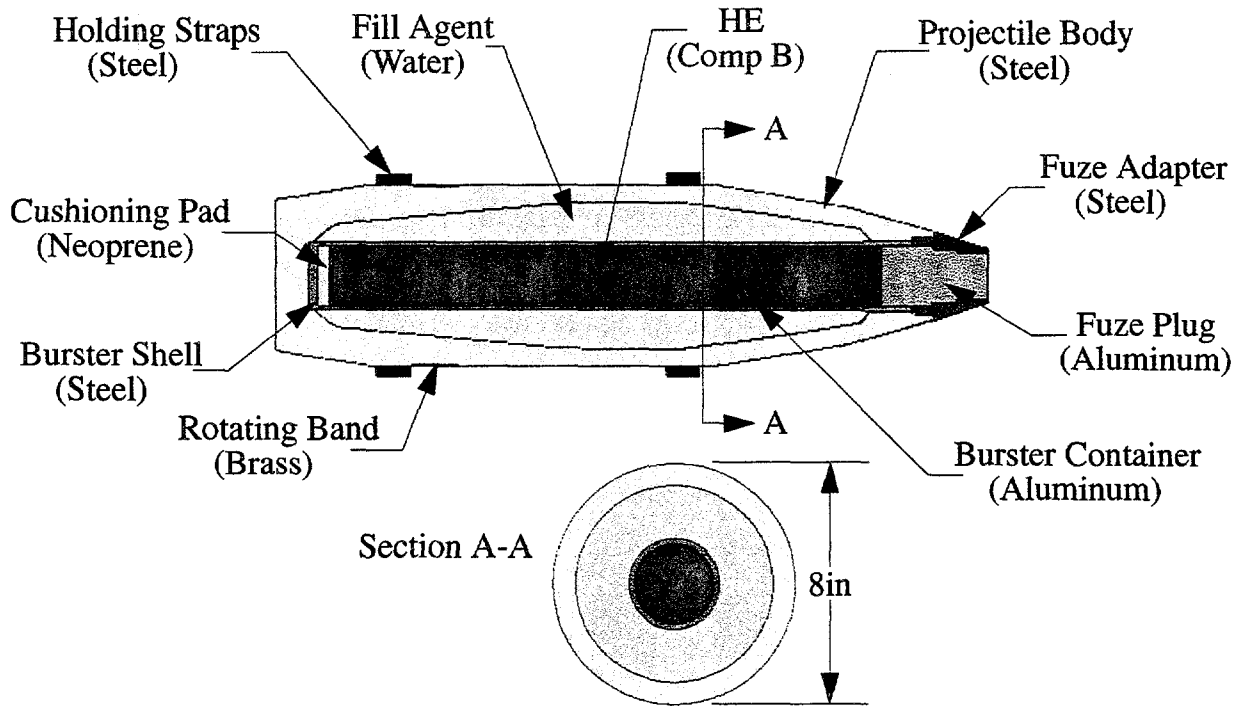

Figure 4. CTH model of the M426 8-inch chemical round.

Table 1: Comparison of Actual and Model Component Masses for M426

Munition Component	Actual Mass (kg)	CTH Model Mass (kg)
Explosive (Comp B)	3.17	3.08
Agent Fill	6.58	7.11
Projectile Body (Steel)	69.75	77.76

A model of the M426 munition located in the APV is shown in Figure 5. As noted earlier, the paths where case fragments would encounter the least mass are critical, so the APV was modeled without any appendages. The structural assembly of the APV, with internal and external rails, etc. all contribute to reducing fragment velocities, but there are some regions where only the 3/8 inch APV wall stands between the munition and the ECC. The strain to failure for the munition case

steel ranges from 15 - 30% (Picatinny Arsenal, 1962b). The expansion space between the munition case and the APV, 2 inches, can accommodate about 50% circumferential strain in the munition case, so it is expected that substantial fragmentation will have occurred by the time the case material impacts the wall of the APV.

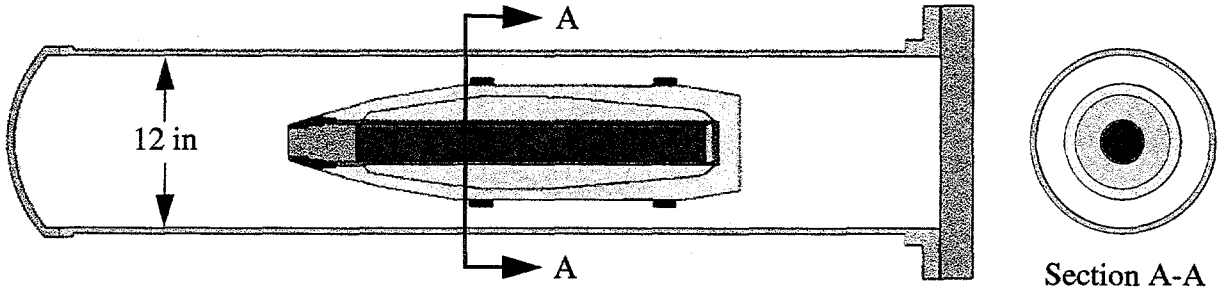

Figure 5. CTH model of the M426 8-inch chemical round located in a model of the APV.

Under field recovery conditions, it is possible that the munition will not be found in the pristine condition as represented in Figure 3 and Figure 4. Rather, part of the case may have been corroded away, and agent leakage may have occurred. The approach to such a scenario has been to include in the analyses a munition with a case thickness that is half of the pristine condition, with and without the agent present. Also, a detonation of the charge in a pristine munition after the agent has been drained was evaluated. Simulations discussed in Appendix E illustrate the consequences of such mass alterations to the original device, and the effect on the fragment characteristics (velocity and dimension).

III. CTH CODE NUMERICAL ANALYSES

The initial analysis task is to determine the case fragment characteristics - dimensions and velocities - as the case expands from the burster charge detonation. Fragments will interact with the APV wall (3/8 inch stainless steel), then impact the ECC 30 mm inner steel wall after a free flight distance of approximately 1 m. The focus is on defining the largest realistic fragment mass and its associated velocity. Expanding cases from explosive charges have been extensively studied (e.g., Mott, 1943; Mock and Holt, 1983). It has been shown that an accurate measure of the average fragment size can be related to the expansion strain rate (Grady, 1988), and that Poisson statistics provide a good description of the statistical distribution of sizes about the mean (Grady and Kipp, 1985).

The following analyses address the case expansion in two representations, with the intent to determine fragment characteristics from both circumferential and axial breakup, including interaction of the munition case with the APV: (1) normal function axial detonation of the munition explosive within the APV, and (2) detonation of the explosive in a transverse cross-section of the munition and APV, where statistics about a mean case fragment dimension determined in the previous step are applied. Variations of the munition that include possible corroded case and extent of agent fill were also made to ensure that extremes of fragment velocities and sizes have been obtained, and are described in Appendix E. Monitoring local case and APV response to the explosive loading is accomplished with massless tracer particles attached to material at selected positions. After the fragment(s) have been characterized, impact onto the ECC is addressed. Idealized and realistic fragments are employed to ascertain the vulnerability of the ECC to such incidents.

Most of the simulations reported here are two-dimensional, with the exception of a limited number of three-dimensional fragment impacts onto the ECC. All two-dimensional calculations have been made with a uniform resolution of at least 1 mm. A few were made with a finer uniform resolution of 0.5 mm in order to specifically ascertain the effects of numerical resolution on fracture process. These results are discussed in Appendix D. The three-dimensional simulations had a uniform resolution of 2 mm.

A. Fragment Characterization from an Exploding Munition

When the M426 munition is detonated in the APV under normal function conditions, the explosive burster charge is initiated at the nose, and the munition responds as shown in Figure 6. The detonation front travels along the axis at about 8 km/s, and the reaction is complete after 76 μs. Note that in regions where the case is thick (near the projectile base), the initial shock transmitted through the chemical agent to the case is of sufficient amplitude to cause internal fractures (spall) in the steel. The chemical agent is also drawn into tension after the case begins to expand, resulting in either vapor formation or dispersed liquid. The expanding case first impacts the APV approximately 150 μs after explosive initiation. One notable aspect of the munition case expansion is the degradation that follows impact with the APV wall: the thinner APV wall causes internal fracture (spallation) within the case over nearly its entire length, except for part of the aft region. This fracture effectively reduces the case fragment thicknesses.

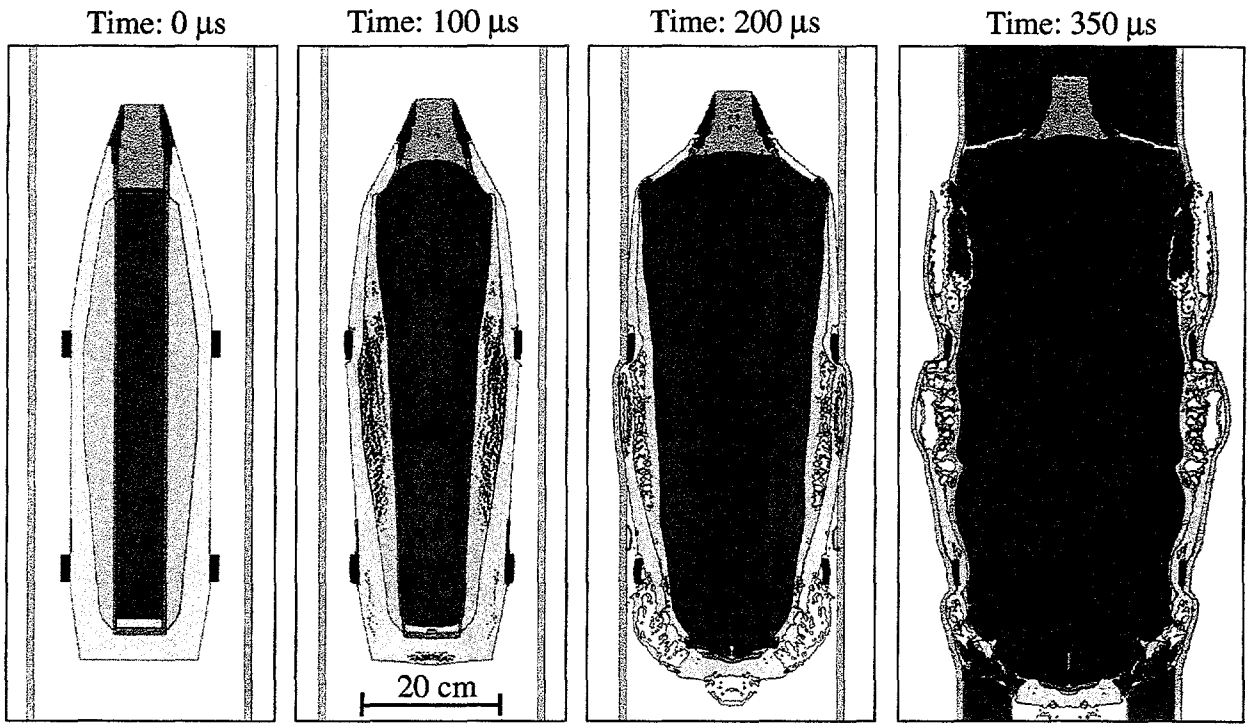

Figure 6. CTH calculation of normal burster charge function (fuze-end initiated) for the M426 8 inch chemical round; 100% agent fill.

The local maxima of case expansion velocity (prior to impact with the APV) are plotted in Figure 7 as a function of axial position.The lowest velocities are located towards the aft end of the projectile, where the case is thickest. The largest velocity, about 520 m/s, occurs in the forward, thinner case section where the least chemical agent is present, and the explosive coupling to the case is more direct. The clamps clearly act to retard local motion (near tracers 6 and 13).

The axial and circumferential strains are monitored at these same locations to determine when the munition will fail, and the strain rates at the time of failure are used to estimate the characteristic fragment dimensions (see Appendix A). Axial strains in the munition were obtained by monitoring the motion of adjacent tracer positions. Almost without exception, these axial strains were much less than 15% by the time the case impacted the APV. Although these axial strains on average are insufficient to clearly cause fracture, there are local fractures that develop in the vicinity of the clamps (Figure 8). The APV provides two fairly well-defined fragment characteristic lengths (19 - 26 cm), with thicknesses of 5 - 8 mm, and the aft case is a source of one large characteristic length (16 cm), with thickness ranging from approximately 9 - 22 mm. The axial extension strain rates along the case range from 300 to 800 /s, which correspond to fragment characteristic sizes of 7 to 24 cm. The larger length is consistent with the maximum size observed in Figure 8. In addition to the breakup that occurs when the munition case impacts the APV, a substantial velocity reduction is also imposed on the case as the APV is accelerated (compare Figure 7 and Figure 8). Mass averaging the terminal velocities along the case fragment (Figure 8) leads to an average velocity of approximately 300 m/s. Similarly, the APV fragments have average

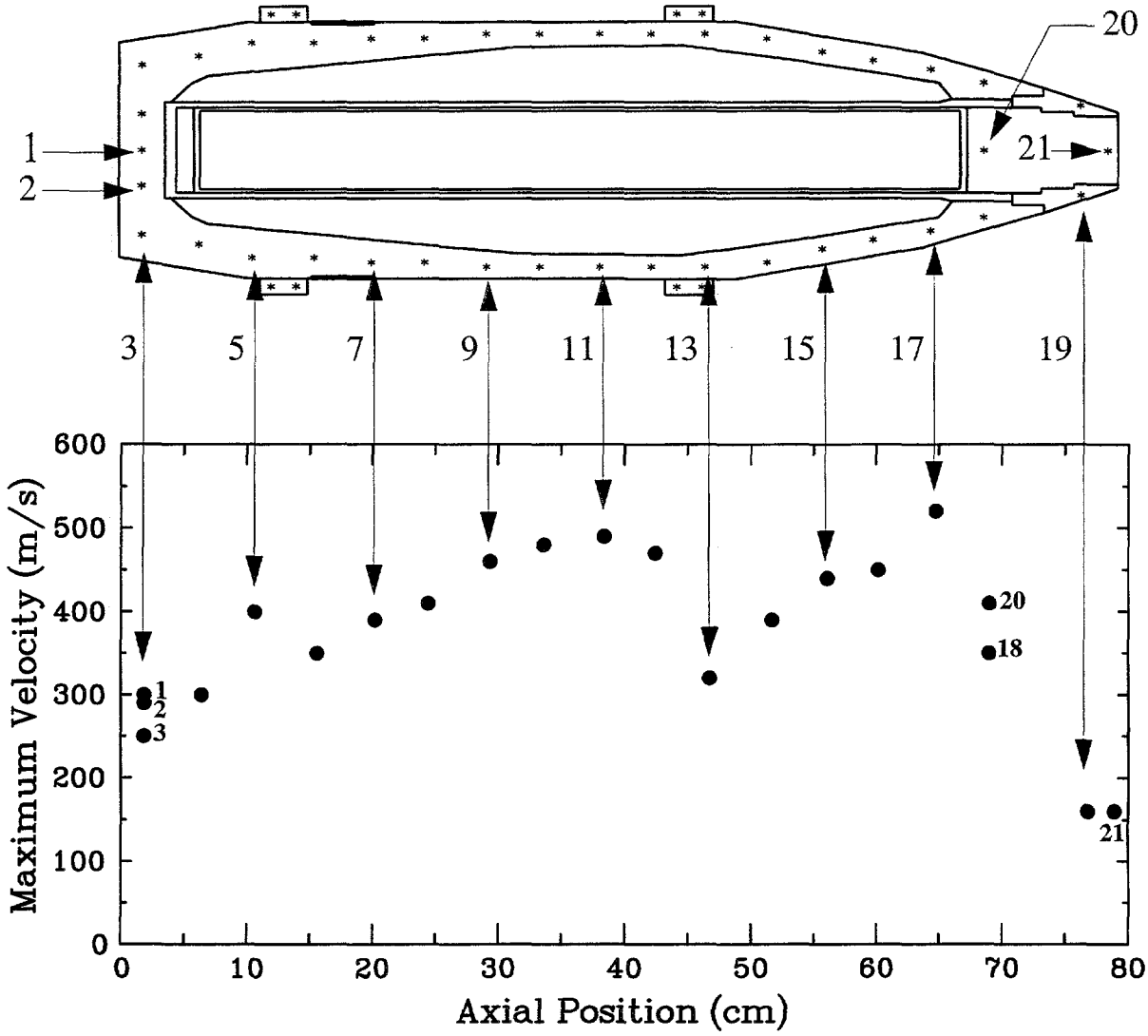

Figure 7. Maximum free expansion case velocities for the M426 8-inch chemical round, normal explosive function initiated; 100% agent fill. Numbers refer to history tracer particles in the munition case.

velocities between 300 and 315 m/s. Further breakup of these fragments would lead to shorter lengths and, as the local momentum is repartitioned, some slower and some faster fragment average velocities would emerge. These same velocity gradients along the fragment contribute to initial angular velocities, and rotation rates of approximately 1000 rad/s result. Average velocities of 300 m/s from APV to ECC give a transit time of about 3 ms; in this interval of time, at least 180 degrees of rotation is feasible. The implication of such rotations is that normal impacts of the fragment in a penetrator configuration onto the ECC wall must be considered in the analyses.

Having acquired estimates of fragment lengths and thicknesses from the simulations of the detonating munition and axial breakup, it remains to define a characteristic width from the circumferential breakup of the munition case and APV wall.

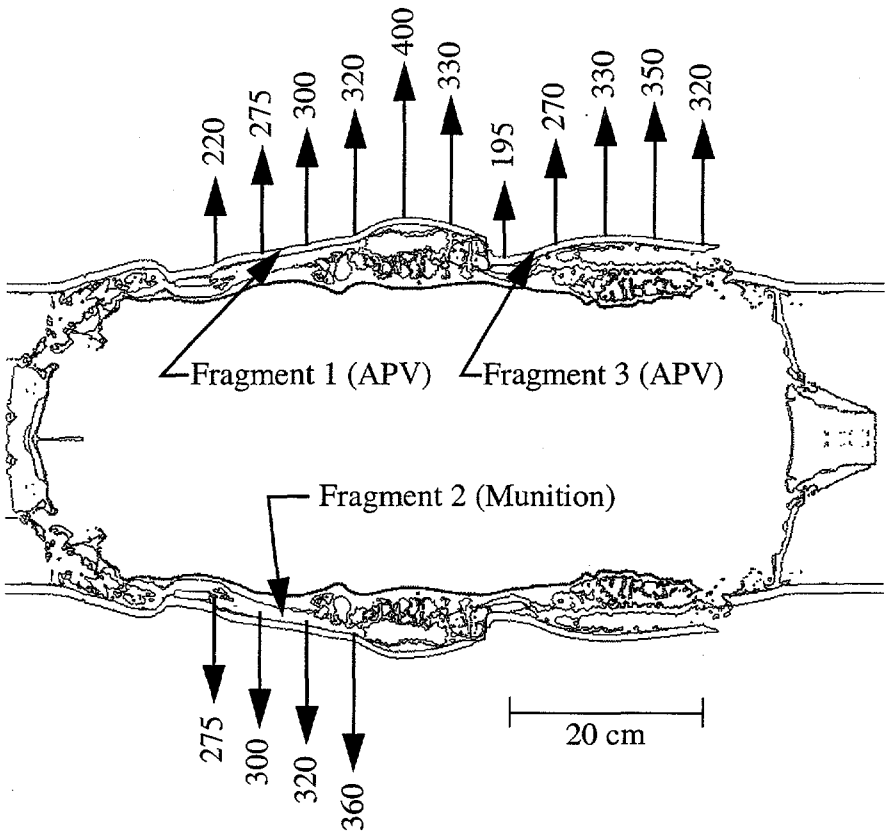

Figure 8. Definition of three major fragments and associated radial velocities (m/s) in the expanded APV and munition case (350 μs).

An example of circumferential strain rate (determined from the case expansion velocity divided by the radius) as a function of circumferential strain is shown in Figure 9 (left) for a position forward of the axial center of the munition. Assuming that fracture occurs by about 15% strain, the strain rate at the time of fracture is about 4500 s^{-1} (15% circumferential strain corresponds to a case radius of about 12 cm, which is well within the inner APV radius of 15 cm; the corresponding velocity is 490 m/s). The resulting average fragment dimensions, based on the relationships in Appendix A, depend on the fracture toughness for this steel, and range from 20 to 40 mm for this strain rate. The strain rate at fracture varies with axial case location; the plot in Figure 9 (right) includes the average fragment dimension at each of the case tracer locations. The largest average fragment dimension expected is about 55 mm. The dependence on possible fracture toughness extremes is illustrated in this figure. The inverse dependence of the fragment size on the strain rate is clearly reflected in Figure 9, relative to the maximum velocity curve in Figure 7.

In a transverse section of the munition, the circumference of the case midplane at 15% expansion is about 65 cm. Using a characteristic dimension of 45 mm in the circumferential direction as a representative estimate of fragment dimensions, 13 - 14 fragments could be expected to form. Assuming this fragment quantity applies to a transverse section of the munition, 15 random scores are introduced into the inside surface of the steel case to define explicit random

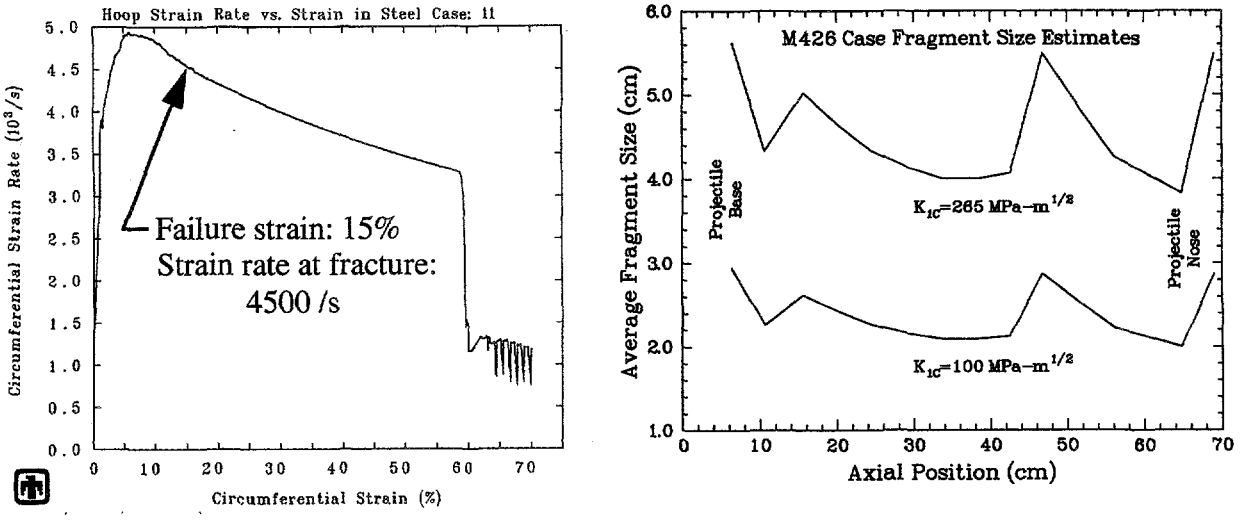

Figure 9. (Left) Circumferential strain rate as a function of circumferential strain at a central position in the munition case.
(Right) Average case fragment dimension as a function of position along the munition for expected extremes in fracture toughness.

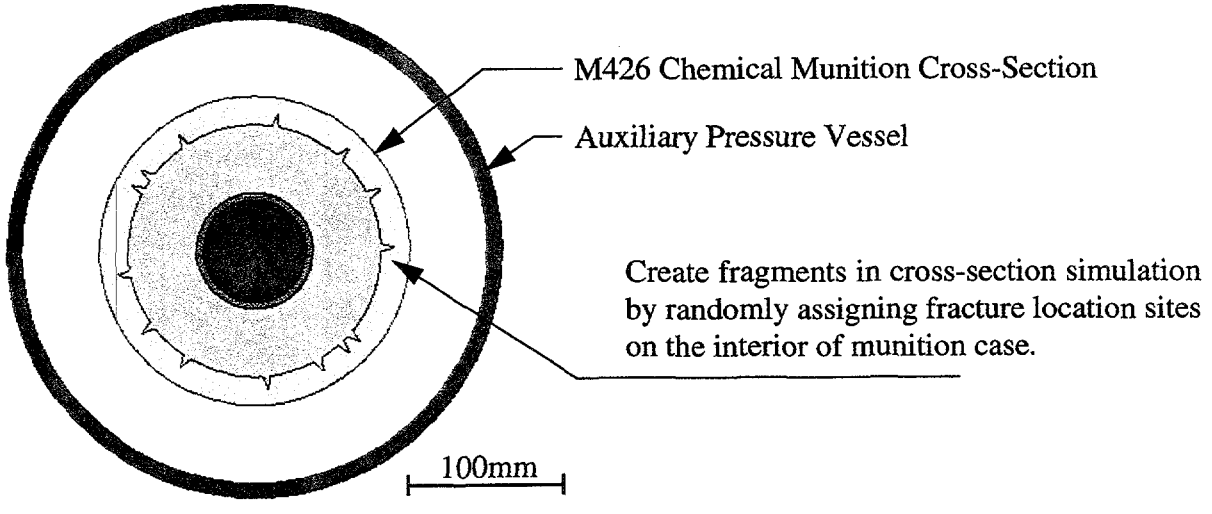

Figure 10. Method of creating fragments by scoring interior of munition case at random locations, based on mean fragment dimension of 45 mm.

fragment lengths with a statistical mean fragment dimension of 45 mm (Figure 10). The intent of the internal scores is to force the case to fragment in a statistically representative manner. The APV is also included in the calculation in order to examine the interaction of the case fragments with the

APV. This is a two-dimensional planar geometry, in which the explosive and surrounding materials are modeled as cylinders of infinite extent.

When the burster explosive is detonated in this transverse section of the munition (near the munition axial center) and APV, the expansion proceeds as shown in Figure 11. Under these circumstances, the explosive requires only 4 μs to complete detonation. By 50 μs the case fractures appear to have grown nearly through to the exterior, and by 100 μs the fractures are complete, resulting in distinct fragments moving towards the APV. The chemical agent (water) undergoes cavitation as in the axial simulations. Shortly after 100 μs the fragments impact the wall (at normal incidence) creating pressures in excess of 50 kb. The APV wall (9.5 mm) is thinner than the case fragment at impact (~16 mm), with the consequence that the planar impact leads to internal tension in the fragment, causing a classical spall to form lengthwise across the fragment, clearly seen at 150 μs. The case fragments have severely distorted the APV by 200 μs, and by 250 μs the case fragments have broken through the APV; the outer half of the fragment retains the same acquired velocity as the APV, and the inner half lags behind. Depending on the location and initial size of the case fragment, accelerated APV fragments can be seen to further break in the circumferential direction. An important consequence reinforced in this view of the expansion is that the original case fragments appear to lose their integrity during impact with the APV, forming a new set of fragments that are substantially thinner than the original case wall thickness. This is consistent with the axial detonation of the munition in the APV (Figure 6). The characteristic circumferential dimensions of the additional fragments formed by the impact of the case onto the APV are no larger than the original case fragments. The largest residual circumferential dimension is about 70 mm, which is about 40% larger than the initial average dimension of 45 mm (a result of the statistics used to generate randomized fragment dimensions, and the additional circumferential strain); the fragment thickness, though, now corresponds to that of the expanded APV wall, about 8 mm (Figure 12). When this geometry is modeled with finer resolution (Figure D3, Appendix D), there are some variations in how the larger APV fragments break up, but the overall final maximum lengths remain unchanged. Another consequence of the original 14 fragments impacting the APV wall is the multiplication of fragments to several times the starting number. By the time that the discrete fragments from the munition have broken through the APV (250 μs), the circumferential strain in the APV wall is only 30%, so large scale extensional failure (requiring 55% strain) does not contribute to the fragmentation of the APV.

The initial velocity imparted to the case in this sectional calculation is about 520 m/s, which is consistent with the case velocities plotted in Figure 7 for the full axial detonation. The momentum transfer that takes place during the fragment impact with the APV is illustrated in Figure 13, where case and APV tracer particle velocity histories are plotted at locations on the negative horizontal axis (arrows). Both the inner and outer tracers in the case are accelerated to an expansion velocity of about 520 m/s. When the case contacts the inner surface of the APV at 125 μs, the fragment velocity is decreased until the APV and the outer case fragment acquire nearly common velocities of 420 m/s; after the spall is complete, the inner case fragment velocity has been reduced to about 250 m/s. These velocities are consistent with the larger terminal velocities shown in Figure 8 for the three major fragments defined there.

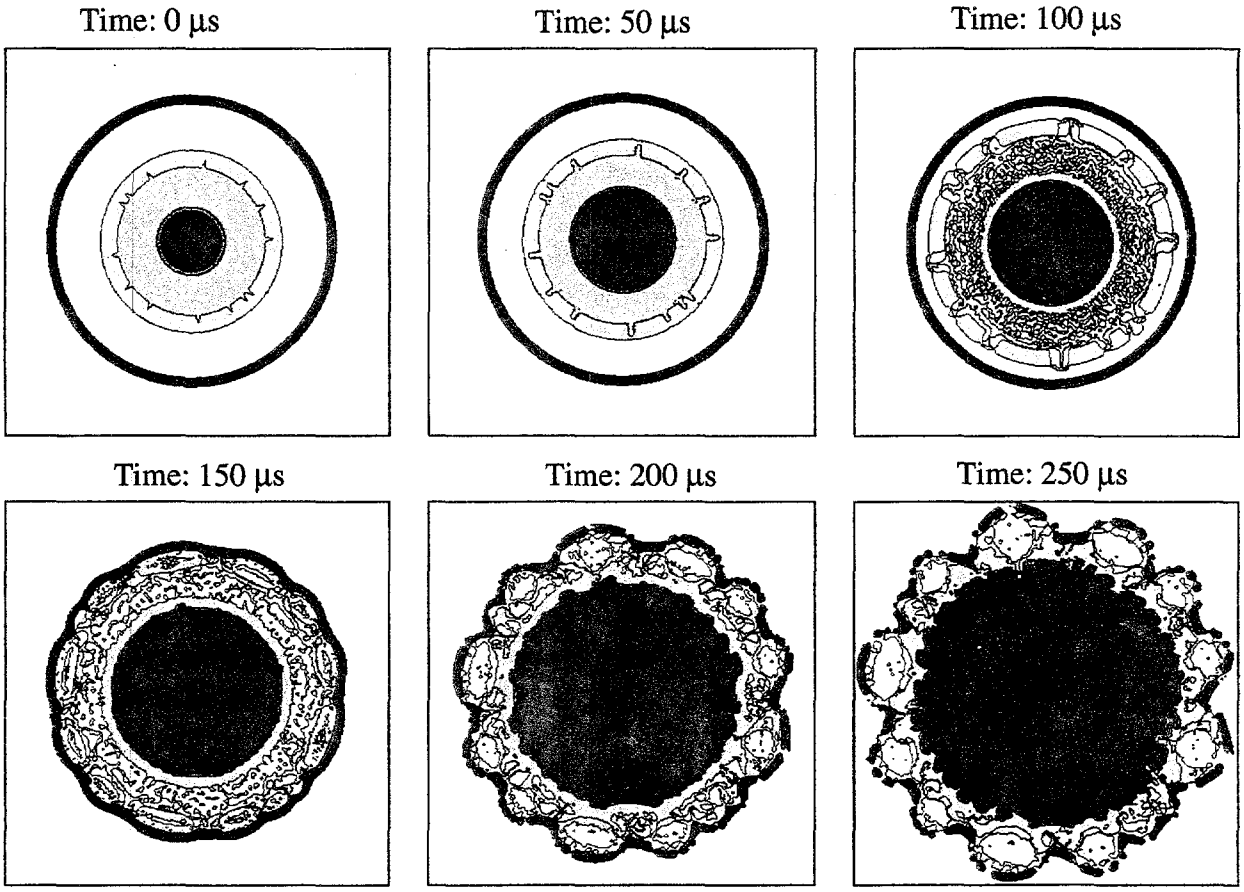

Figure 11. CTH calculation of M426 8-inch chemical round transverse section; 100% agent fill.

From these two simulations - the full munition and a transverse section - major fragments can be defined that result from this accidental detonation of the M426 chemical munition in the APV: lengths of 160-260 mm, widths of 70 mm, and thicknesses of 5 to 22 mm. These nominal ratios of width to length of about 4 are consistent with data from certain explosive shells where nominal length to diameter ratios of 5 or less are common (Mott, 1943). Characteristics of the three major fragments are listed in Table 2, and perspective views of possible configurations of each are shown in Figure 14. A variant on Fragment 1 is included in which the higher-velocity section of the fragment is separated out as a distinct fragment.

These fragment characteristics result from the analysis of a pristine munition. Aged munitions recovered in the field could be found in various stages of decay. A few variations on possible configurations (e.g. corroded (thinned) case, leaked agent), are evaluated in Appendix E, and indicate that the fragment attributes obtained in this section are representative of the largest masses and velocities expected in the event of an accidental detonation. Application of statistical distributions to the fragment length was not made, presuming that those fragments were of the maximum possible length. Instabilities during expansion commonly limit the lengths observed, so the narrower fragments would be expected to have shorter lengths than the wider fragments.

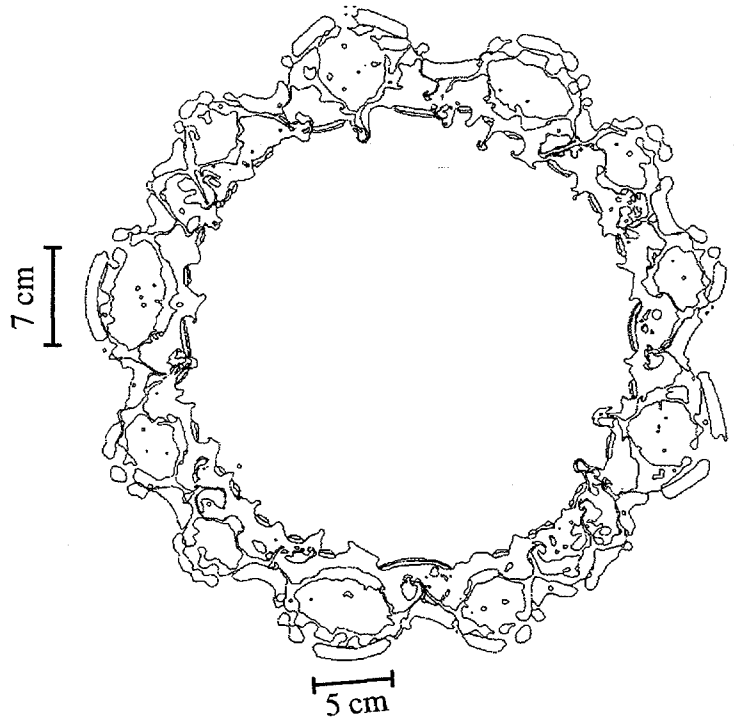

Figure 12. Characteristic dimensions of the largest fragments resulting from transverse section. (Time: 250 μs)

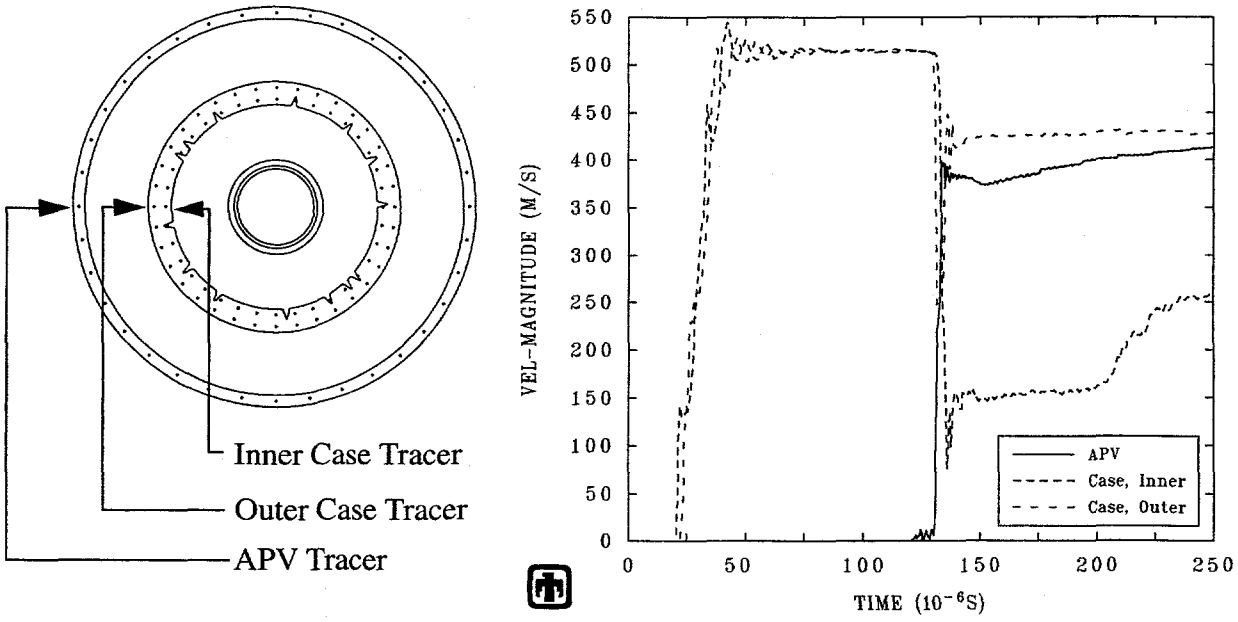

Figure 13. Expansion velocity histories of a case fragment and APV wall.

Table 2: Major Fragment Characteristics

Fragment	Material	Length	Width	Thickness	Mass	Velocity
1	APV SS	26 cm	7 cm	5 - 8 mm	1050 g	315 m/s
1A	APV SS	12 cm	7 cm	5 - 8 mm	450 g	400 m/s
2	Case Steel	16 cm	7 cm	9 - 22 mm	1250 g	300 m/s
3	APV SS	19 cm	7 cm	5 - 8 mm	780 g	300 m/s

Figure 14. Possible configurations of three primary fragments (see Table 2).

B. Fragment Impact on the Explosion Containment Chamber Wall

The vulnerability of the ECC wall structure to the fragments defined in the previous discussion is the topic of this section. Two approaches to fragment impacts onto the chamber wall are pursued: (1) three-dimensional analyses of the fragments illustrated in Figure 14, and (2) two-dimensional idealizations of those fragments as long cylindrical rods. Although the first method captures some aspects characteristic of fragment impact, the typical irregularities associated with explosively formed fragments are not included, and only limited parameter variations can be addressed in three-dimensional analyses. An alternative is to transform the cross-sectional area of the original

fragments into a circular section of equal area, so long-rod axisymmetric simulations can be employed to examine fragment impact onto the ECC. Variations of such idealized fragments can be readily made. In addition, in order to place the simulations into an experimental context, a long-rod impact case was used as a benchmark to check the code accuracy in this limit velocity application (Appendix C): the CTH simulations were found to under-estimate the ballistic limit velocity by about 15%.

The placement of the APV and munition in the ECC is such that the fragments ejected from the munition and APV will impact the cylindrical chamber walls. As described earlier, the large radius of the chamber provides ample time for fragments from a source near the center of the chamber to rotate in flight. Although normal impacts on a local region of this wall are expected to be the most lethal orientation, analysis of a flat impact is also included.

It should be noted here that with a yield strength of 480 MPa, the ECC wall steel is susceptible to local permanent deformation from any steel fragment with an impact velocity in excess of 50 m/s. For steel impacting steel, the shock jump conditions relate the impact stress, σ, to the density, ρ, shock velocity, U_s, and impact velocity, V_{imp}, as

$$\sigma = \rho \cdot U_s \cdot \frac{V_{imp}}{2} \qquad (1)$$

At low impact velocities, the shock velocity is approximated by the longitudinal velocity, about 5 km/s for steel; the density of steel is 7800 kg/m^3, and the stress to reach yield, the Hugoniot Elastic Limit, is related to the yield stress through the Poisson ratio, ν (0.28 for steel),

$$\sigma_{HEL} = Y_0 \cdot \frac{1-\nu}{1-2\nu} \qquad (2)$$

The threshold velocity, then, for the impact stress to equal the yield stress is about 40 m/s. Having determined that the fragment velocities from the exploding munition in the APV are on the order of 300 m/s, substantial local deformation should be expected in the ECC walls at impact sites.

1. Three-Dimensional Impact Simulations

Two of the three fragments defined in Table 2 and Figure 14 - Fragment 2 and Fragment 3 - were chosen as representative of large massive fragments impacting the ECC. Impact with each of these two fragments was first made with the fragments oriented to strike end on at 300 m/s, appearing as a long projectile. In order to include higher velocity fragment impact conditions, one-half of Fragment 1A (450 g) was impacted end on at 400 m/s, which is at the upper end of velocities expected for any part of the fragments defined in Figure 14. Finally, Fragment 2 was oriented to impact on its broadly curved face at 300 m/s. The initial configurations for these four cases are illustrated in Figure 15. The ECC wall structure is defined with a 30 mm inner steel wall (the first to be impacted by the fragment), a 30 mm layer of water / glycol, and a 15 mm external steel wall. Properties of the ECC steels are tabulated in Appendix B. Advantage is taken of the

symmetry plane through the cylindrical axis used to generate the fragment. These CTH simulations were resolved with uniform 2 mm cells.

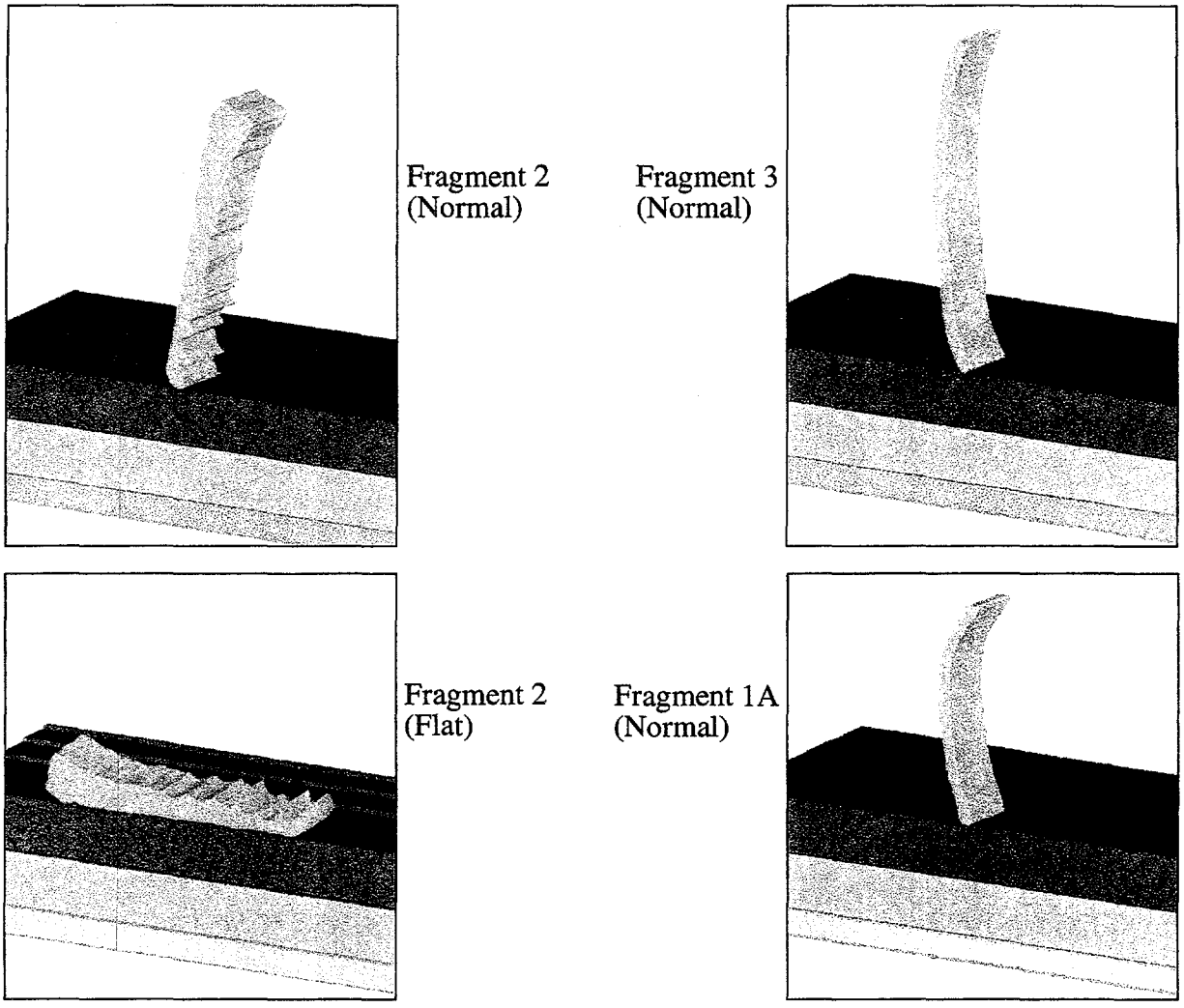

Figure 15. Initial fragment and ECC configurations for three-dimensional analysis. (Shown with 1/2 the full geometry.)

A sequence for the normal impact of Fragment 2 onto a section of the ECC wall is shown in Figure 16, for Fragment 3 in Figure 17, and for Fragment 1A in Figure 18. Perforation does not occur in any of these cases; rather, each fragment causes substantial local deformation on the impact face, and some bowing of the inner wall. The largest bulge in the outer layer forms for the more massive Fragment 2 (Figure 16), although the less massive fragments also result in slight outer wall deformation. Penetration depth is about 8 mm for Fragment 2, about 5 mm for Fragment 3, and about 5 mm for Fragment 1A. In a flat impact orientation, Fragment 2 also generates large deformations (Figure 19), again with about 8 mm of penetration accruing. The velocity of the fragment in this flat orientation is such that the spallation threshold has not yet been reached, so no internal fractures form in the ECC inner wall.

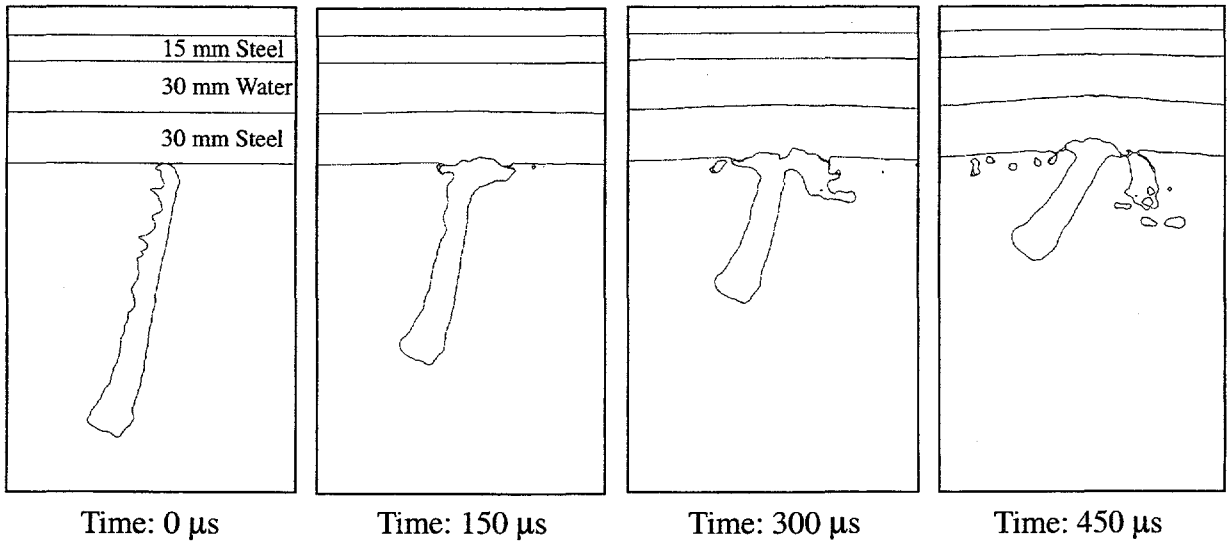

Figure 16. Fragment 2 (1250 g; 300 m/s) normal impact onto the ECC. View is a cross-section in the symmetry plane. Depth of penetration is about 8 mm.

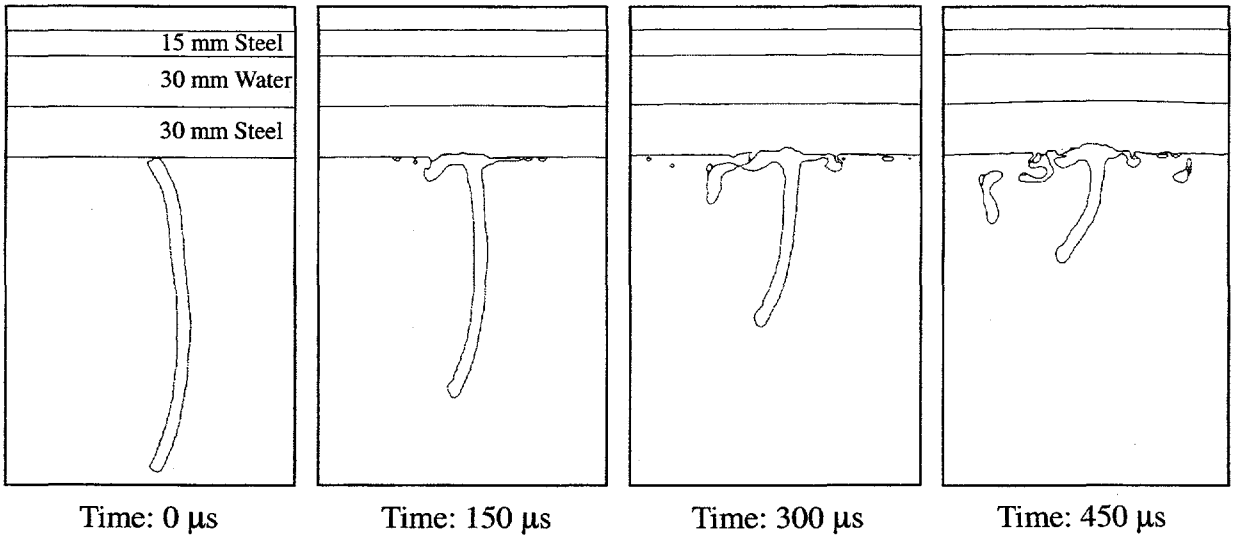

Figure 17. Fragment 3 (780 g; 300 m/s) normal impact onto the ECC. View is a cross-section in the symmetry plane. Depth of penetration is about 5 mm.

(Impact at 350 m/s has also been examined for this flat impact configuration, and no spall occurs at this velocity either.) Although the time durations of the normal impacts are long (nearly 500 μs) because of the length of the projectile relative to its impact velocity, there is not much evidence of fragment buckling during impact; however, all the fragments in normal striking orientation exhibit

slight rotations by the conclusion of the impact simulation (Figure 16, Figure 17, Figure 18). In the case of Fragment 2, at its current rotation rate, approximately 300 μs additional time would be required for the fragment to rotate into the target; and for Fragment 3, at least another 250 μs is required. In neither case will further penetration occur.

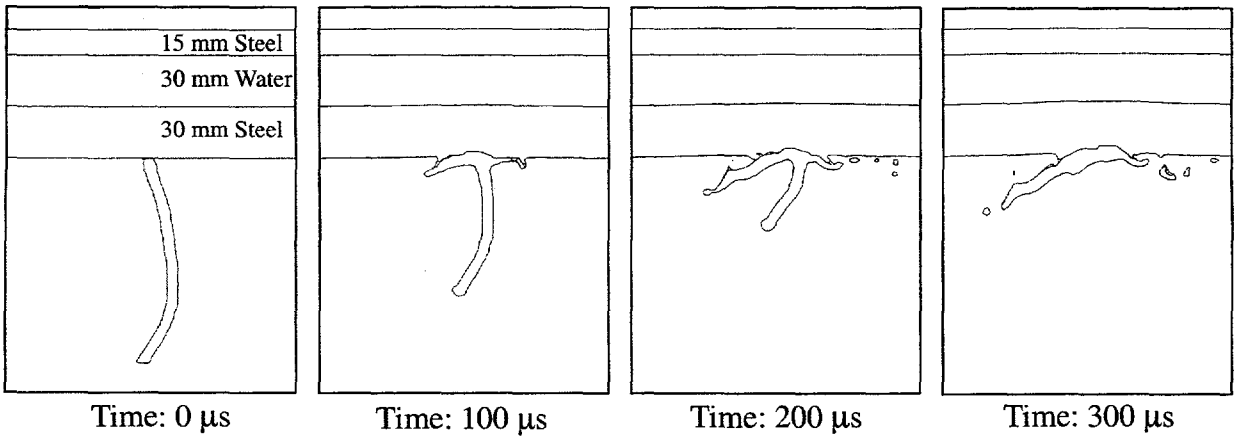

Figure 18. Fragment 1A (450 g, 400 m/s) normal impact onto the ECC. View is a cross-section in the symmetry plane. Depth of penetration is about 5 mm.

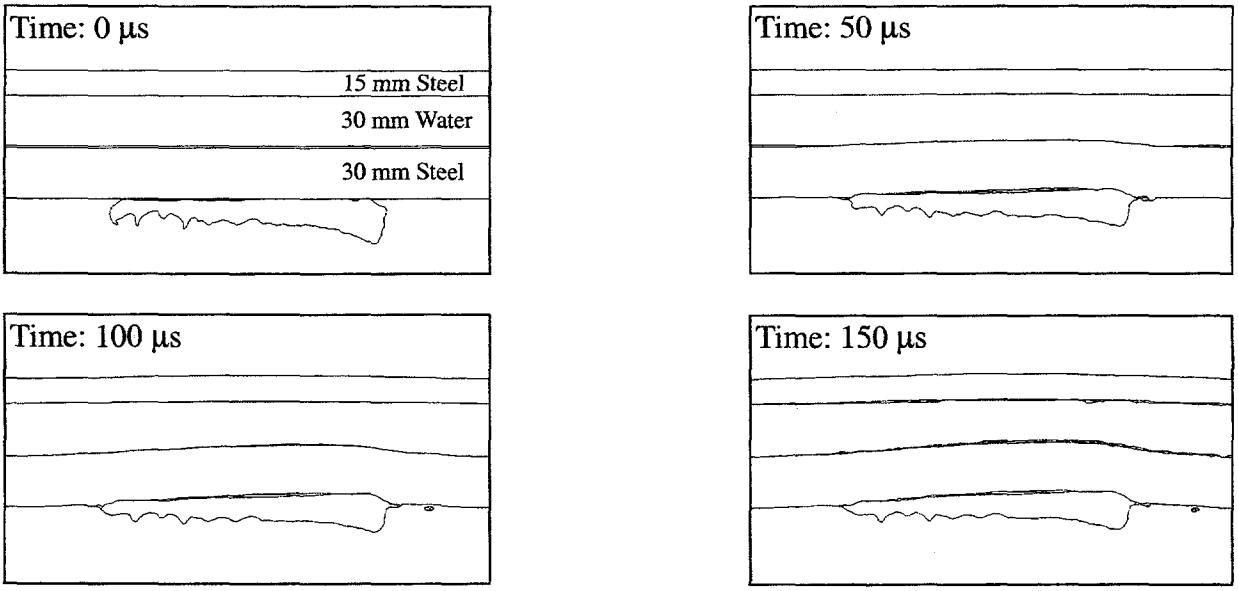

Figure 19. Fragment 2 (1250 g; 300 m/s) flat impact onto the ECC. View is a cross-section in the symmetry plane. Depth of penetration (deformation) is about 8 mm.

2. Two-Dimensional Impact Simulations

Idealized fragments in the form of long cylindrical pointed rods were constructed from the fragments discussed in the previous section, and impacted at normal incidence onto the ECC wall structure. When the fragment cross-section dimensions from Table 2 (width and thickness) are approximated with circular sections, diameters ranging from 21 to 45 mm could be expected, derived from 5 x 70 mm and 22 x 70 mm fragments, respectively. Several other rod diameters in the range of 14 to 36 mm were chosen to impact the target, and to calculate the limit velocity expected from these rod impacts. The ratio of length to diameter was set between 3 and 5, to maintain fragments that were similar in length to the three-dimensional fragments, and to be in accordance with published data (Mott, 1943). Consequently, the masses of the rods are equal to or less than those of the three-dimensional fragments from which the cross-sections were determined.

An example of the impact of an axisymmetric cylinder (equivalent in mass to Fragment 2, the largest fragment) onto the ECC wall is shown in Figure 20, where the projectile is a 36mm diameter pointed rod of length 16.8 cm (length to diameter ratio of 4.67) and 1250 g mass. The rod penetration is terminated rather quickly, although there is considerable mushrooming of the projectile steel in the region of impact, and extensive plate deformation. Total penetration is approximately 11 mm, which is about 35% more than that of the three-dimensional fragment which it is intended to represent. The impact sequence of the rod equivalent to Fragment 3 is shown in Figure 21. In this case, the fragment penetration is about 6 mm, which is 20% greater than the three-dimensional fragment it represents. When compared to the larger fragment in Figure 20, the rear surface bulge caused by this fragment is much reduced.

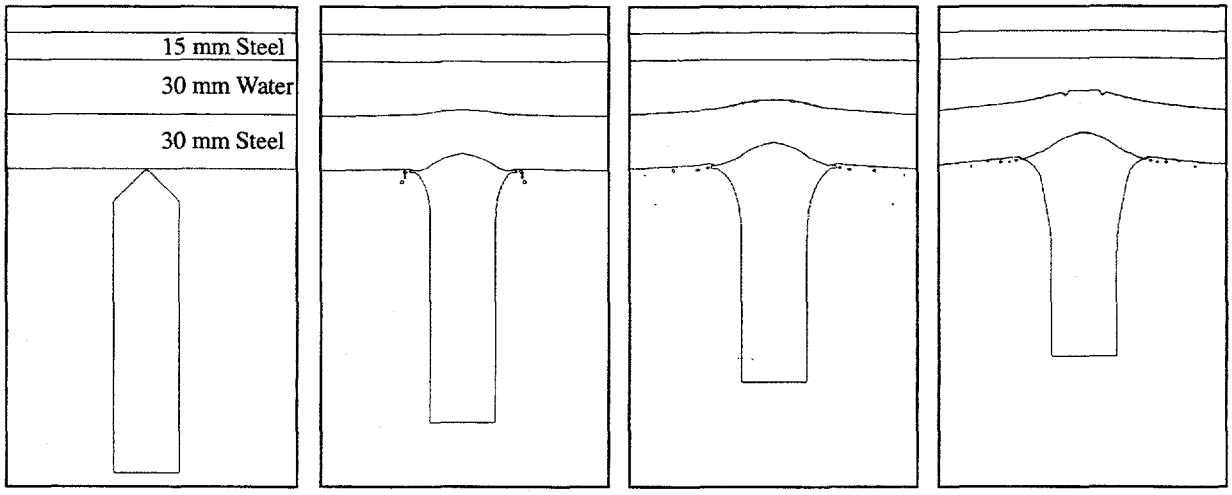

Figure 20. Sequence of long rod equivalent to Fragment 2 normal impact (300 m/s) onto the ECC. Depth of penetration is about 11 mm.

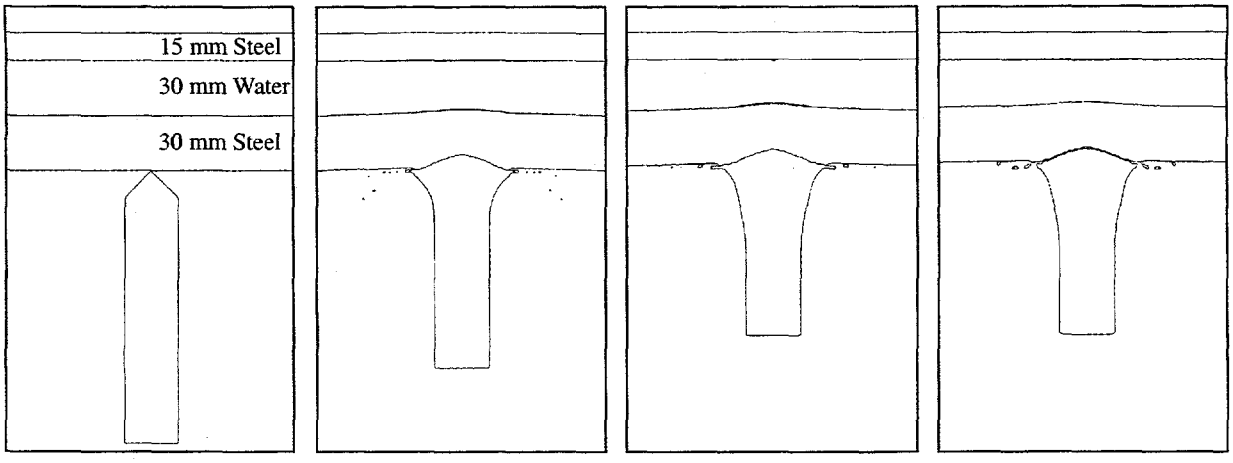

Figure 21. Sequence of long rod equivalent to Fragment 3 normal impact (300 m/s) onto the ECC. Depth of penetration is about 6 mm.

A summary of results for the fragment and rod impacts is shown in Figure 22, where the fragment velocity and fragment mass are the coordinates, and some CTH points with depth of penetration are noted. Recalling the depths of penetration for the more massive three-dimensional fragments (Table 2), the rods tend to penetrate to larger depths, effectively being more lethal than their original counterparts, where depths of penetration were limited to about 8 mm. In some cases, rod impact parameters were chosen to complement on-going ConWep analyses, so a selection of fragment masses and impact velocities were calculated with CTH. These results are summarized in the Discussion (Section V).

Limit velocity curves for long rods are also plotted in Figure 22 for this target, based on both CTH simulations and the empirical limit velocity expression described in Appendix C. In Appendix C, it is shown, for a single example, that CTH tends to calculate a penetration at a given velocity that is too large by about 15%. The limit velocities from Equation C3 are larger than the CTH calculations at all impact conditions included here, consistent with the under-prediction of limit velocity by CTH. Table 3 includes the parameters for these limit velocity cases for the target thickness, t, of 30 mm (L, projectile length, D, projectile diameter). The final column in the table is the % difference that CTH underestimates the empirical results. It should be noted that the coefficient for the empirical curve is based on projectile and target yield strength parameters that are higher than the values for the application here (compare Table B3, Appendix B, and Table C2, Appendix C). The absence of water in the empirical calculations is considered immaterial.

Table 3: Summary of Limit Velocity Curve Points (30 mm target)

L (cm)	D (cm)	L/D	t/D	Mass (g)	V_{lim} (CTH)	V_{lim} (Eq. C3)	% Diff.
5.71	1.43	4.0	2.10	66	780	1021	24
8.0	2.8	2.86	1.07	342	540	705	24
10.0	3.0	3.33	1.0	500	500	618	19
15.0	3.0	5.0	1.0	777	475	505	6
16.8	3.6	4.67	0.83	1246	425	451	6

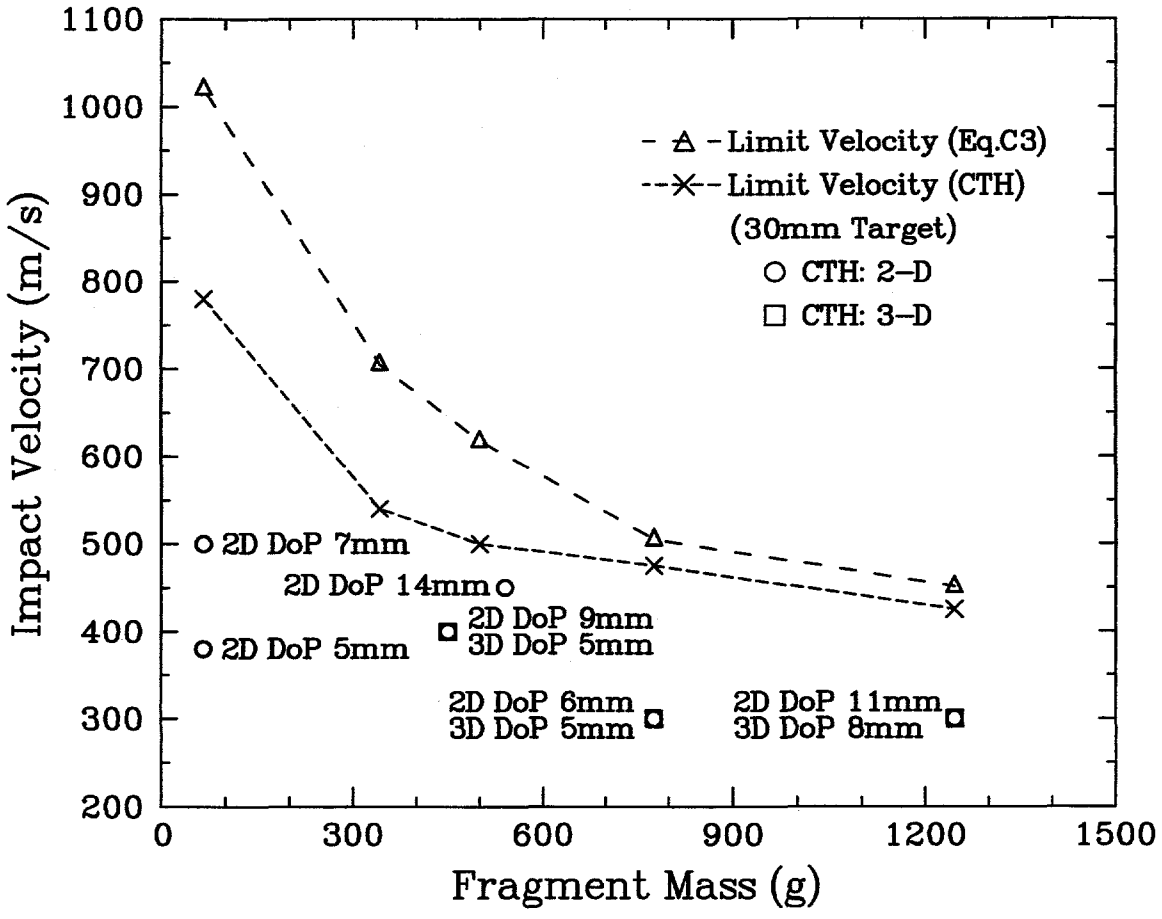

Figure 22. Analytic and numerical (CTH) limit velocity curves, and depth of penetration for long rod and three-dimensional fragment impacts onto the ECC wall.

IV. GURNEY AND ConWep ANALYSES

An independent means of assessing case expansion velocities utilized the Gurney method (Jones, et al., 1980; Kennedy, 1970). A complementary approach to analyze the vulnerability of the ECC to fragment impact is to use a conventional weapons effects code, ConWep, that draws upon an extensive database of explosive fragment formation and impact onto targets.

A. Gurney Analysis

The Gurney calculation is an analytic method developed for calculating approximate speeds of fragments dispersed by high explosive charges. The equations are based on the assumption that the potential energy available in the high explosive before detonation is equal to the kinetic energies of the detonation product gases and inert material after detonation and expansion. Gurney made the assumption that the gaseous detonation products remain uniformly dense during expansion. Formulas are available for a variety of simple configurations in which the explosive is in contact with the inert materials that are explosively formed into fragments.

For cylindrical configurations, the fragment velocity is given by the following equation:

$$V = [2 \cdot E]^{1/2}\left[\frac{M}{C} + \frac{1}{2}\right]^{-1/2} \qquad (3)$$

where V is the fragment velocity, $[2 \cdot E]^{1/2}$ is the Gurney characteristic velocity for a given explosive, M is the mass of the surrounding inert material, and C is the mass of the explosive.

For a Gurney calculation on the chemical munition (M426 8 inch artillery shell) of interest here, the liquid agent was considered part of the case and its mass was added to that mass of the inner aluminum and steel shells and the outer steel case. Two Gurney calculations were done. The first used the total munition component weights (168 lb projectile body and liquid, 7 lb Comp B). The velocity from this Gurney calculation was 1778 fps (542 m/s). For the second Gurney calculation, the component masses were calculated assuming a cylindrical configuration with the dimensions measured in the forward region where the steel case is thinnest. With this modified configuration, the Gurney calculation for a cylindrically cased explosive yielded fragment velocities of 1884 fps (574 m/s). These velocities are in good accord with the ones determined from CTH in the forward region of the projectile (*cf.* Figure 7).

B. ConWep Analysis

An estimate of fragment velocity and penetration into targets can be obtained by using the Conventional Weapons Effects (ConWep) computer program. This program incorporates the equations and curves presented in manual TM5-855-1 (including Gurney equations). This computer program was used to calculate fragment velocities and penetration into the APV and ECC; ConWep requires input on the charge and case weights, case thickness, length of assembled weapon, the distance to the target, and the target configuration (including Brinell hardness, BHN).

The liquid agent and the case weights and thicknesses were required to be treated as a single unit. The APV and ECC were conservatively modeled as a single composite spaced target 0.33 ft away. The Brinell hardness was calculated from the tensile strength using the equation:

$$BHN = 1.979 \cdot [TensileStrength(ksi)] + 11.24 \qquad (4)$$

The BHN was calculated to be 166 for the APV and 198 for the steel (Weldox 500) of the ECC.

ConWep calculations were done for the total munition component masses as well as for the scenario of half the outer steel case eroded away. The ConWep results are summarized in Table 4.

Table 4: Summary of ConWep Fragment Results

Configuration	Case Weight	Comp B Weight	Case Thickness*	Fragment Weight	Initial Fragment Velocity	Fragment Velocity After APV Penetration	Penetration into First ECC Layer
Full Case / 100% Agent	168 lb (76.32 kg)	7.0 lb (3.17 kg)	2.79 in (7.09 cm)	20.07 oz (569 g)	1778 fps (542 m/s)	1341 fps (409 m/s)	0.72 in (18.3 mm)
Half Case / 100% Agent	91.3 lb (41.45 kg)	7.0 lb (3.17 kg)	2.21 in (5.61 cm)	10.75 oz (305 gm)	2391 fps (729 m/s)	1773 fps (540 m/s)	0.83 in (21.0 mm)

* Note that this dimension includes both the agent and munition case thicknesses

Initial case fragment velocities for both ConWep configurations are in good agreement with those of CTH (Appendix E, Figure E3, Figure E6). One of the drawbacks of the ConWep code is that it primarily addresses conventional explosive shells rather than ones only partially loaded with explosive and containing other inert masses located between the explosive and the case, as in the present example. In addition, despite the near proximity of the APV to the munition, fragments are presumed to penetrate the APV as if it were a normal target, so the residual velocities do not reflect the extent of the degradation caused by the APV presence. Note also that ConWep evaluates the half munition case, 100% agent fill configuration as more damaging than the pristine condition, primarily because of the large impact velocity.

C. ConWep / CTH Code Analysis Comparisons

The following table summarizes the ConWep and CTH fragment characteristics and impact calculations. One of the areas where ConWep and CTH fail to agree is on the initial fragment mass. The CTH analyses led to munition fragments that were as much as twice the mass of those from ConWep, primarily due to source location: CTH analyses indicated the aft region as the most reasonable munition fragment source; further forward, the APV fragments formed by the impacting case were more important. Although the initial munition velocities agree well prior to

impact with the APV (compare maximum munition velocities in Appendix E, Figure E3, Figure E6 with entries 1 and 2 in Table 5), velocities after impact with the APV are considerably smaller for CTH than for ConWep, affecting the determination of ECC wall penetration depth. ConWep predicts penetration depths up to about two-thirds of the inner wall thickness, nearly twice the maximum that the numerical analyses indicate.

Table 5: Summary of Fragment Calculations

Fragment	Fragment Source	Code	Mass (g)	Length, Diameter (cm)	L/D Ratio	Initial Velocity (m/s)	Velocity after APV (m/s)	Penetration into ECC (mm)
1	Munition	ConWep	569	- / -	-	542	409	18.3
2	Munition	ConWep	305	- / -	-	729	540	21.0
3	Munition	CTH, 3D	1250	16 / 7	2.3	400	300	8
4	Munition	CTH, 3D	1250	16 / 7	2.3	400	300	8 (flat)
5	APV	CTH, 3D	780	19 / 7	2.7	-	300	5
6	APV	CTH, 3D	450	12 / 7	1.7	-	400	5
7	Munition	CTH, 2D	1250	16.8 / 3.6	4.7	400	300	11
8	APV	CTH, 2D	780	15 / 3	5	-	300	6
9	APV	CTH, 2D	450	12 / 2.6	4.7	-	400	9
10	Munition	CTH, 2D	540	16 / 2.4	6.7	-	450	14
11	Munition	CTH, 2D	66	5.7 / 1.43	4	-	500	7
12	Munition	CTH, 2D	66	5.7 / 1.43	4	-	380	5

V. DISCUSSION OF RESULTS

All the analyses made for this study indicate that the ECC will not be perforated by any of the fragments from an accidental detonation of an explosive munition, represented here by the M426 round, when contained within the APV. Damaging penetrations, however, may need remediation so later strikes cannot perforate the ECC inner wall. (The fragment field is diverging, so multiple large fragment strikes at the same position are not likely in a given event). Large fragments with velocities of 300 to 400 m/s can be expected from such an accident, velocities at which substantial local permanent deformation will occur at the impact sites. The fragments formed at the aft end of the munition, where the case has its greatest thickness, cause the most deformation of the inner ECC wall, but less massive, faster fragments penetrate to larger depths. Both the two-dimensional and three-dimensional CTH numerical analyses indicate that significant penetration will occur, to about one-half of the inner (30 mm) wall thickness. In general, the three-dimensional fragments penetrated less deeply than their two-dimensional rod equivalents. In many cases, the shocks transmitted through the glycol / water layer permanently deform the outer ECC wall as well.

When the effects of munition condition (corrosion, agent presence) were evaluated (Appendix E), the resulting fragment characteristics were found to generally be bounded by the fragments discussed in the body of this report for the pristine munition fully charged with agent. This is in large part due to the fragment velocity mitigation afforded by the APV wall. When the agent is removed, the burster explosive products undergo some initial expansion prior to engaging the munition case, resulting in less efficient acceleration of the case, and lower terminal velocities.

As noted in the descriptions of the Auxiliary Pressure Vessel and Explosive Containment Chamber, there are substantial structural and functional elements attached to the APV and within the ECC. This supplemental mass would further reduce the munition fragment velocities, and alter the formation of APV wall fragments over large azimuthal regions where the expanding munition fragments would impact. The focus of this study has been on the clear paths that exist from the detonating munition through the APV wall to the ECC structure. The APV is a critical intervening structure between the munition and the ECC. Limited analyses of munition detonation without the APV present indicate that some munition spall fragments form that have sufficient mass and velocity to perforate the inner wall of the ECC.

This study has identified large fragment masses from the munition and APV as the most lethal objects formed in the accidental detonation of the burster charge. The strain rate magnitudes govern the average munition fragment dimensions as the case expands, and statistical measures were applied to these averages to arrive at the characteristic dimensions of the largest expected fragment. Independent confirmation that these fragment sizes are indeed the largest that could form from this event might be found in arena test data, which was not available for this study.

Limited comparisons of numerical simulations with Gurney velocity and independent penetration data indicate that the code provides accurate measures of the expansion velocities, but tends to overpredict the extent of penetration at a given impact velocity. Consequently, the results reported here are considered worst-case evaluations of the vulnerability of the ECC to accidental detonation of munitions in the APV during remediation.

VI. REFERENCES

Anderson, C. E., B. L. Morris, and D. L. Littlefield (1992). "A Penetration Mechanics Database", Southwest Research Institute Report 3593/001, January 1992.

ASM Metals Progress Databook (1976). Internal reference to Stainless Steels, Universal-Cyclops Specialty Steel Div., Cyclops Corp.

ConWep computer code, U.S. Army Corps of Engineers, May 1989.

Dobratz, B. M. and P. C. Crawford (1985). "LLNL Explosives Handbook. Properties of Chemical Explosives and Explosive Simulants", Lawrence Livermore National Laboratory Report, UCRL-52997, Change 2, January 1985.

"Fundamentals of Protective Design for Conventional Weapons", TM 5-855-1, November 1986.

Gillich, W. (1975). Private communication from Ballistic Research Laboratories to L. D. Bertholf, Sandia National Laboratories.

Grabarek, C. L. (1971). "Penetration of Armor by Steel and High Density Penetrators", Memorandum Report No. 2134, U. S. Army Ballistic Research Laboratory, Aberdeen Proving Ground, MD.

Grady, D. E. (1988). "The Spall Strength of Condensed Matter", *J. Mech. Phys. Solids*, 36, 353-384.

Grady, D. E. (1996). "Spall and Fragmentation in High-Temperature Metals", in *High-Pressure Shock Compression of Solids II*, Ed. L. Davison, et al., Springer, New York.

Grady, D. E. and M. E. Kipp (1985). "Geometric Statistics and Dynamic Fragmentation", *J. Appl. Phys.*, 58, 1210-1222.

Group GMX-6 (1969). "Selected Hugoniots", Los Alamos Scientific Laboratory Report LA-4167-MS.

Hixson, R. S., R. G. McQueen, and J. N. Fritz (1993). "The Shock Hugoniot of 316SS and Sound Velocity Measurements", High Pressure Science and Technology - 1993, Ed. S. C. Schmidt, et al., AIP Conference Proceedings 309, New York.

Hohler, V. and A. Stilp (1987). "Hypervelocity Impact of Rod Projectiles with L/D from 1 to 32", *Int. J. Impact Engng.*, 5, 323-331.

Jones, G. E., J. E. Kennedy, and L. D. Bertholf (1980). "Ballistics Calculations of R. W. Gurney", *Am. J. Phys.*, 48, 264-269.

Kennedy, J. E. (1970). "Gurney Energy of Explosives: Estimation of the Velocity and Impulse Imparted to Driven Metal", Sandia Laboratories Report SC-RR-70-790, December.

Kipp, M. E., D. E. Grady, and J. W. Swegle (1993). "Experimental and Numerical Studies of High-Velocity Impact Fragmentation", Sandia National Laboratories Report, SAND93-0773, August 1993.

Kohn, B. J. (1969). "Compilation of Hugoniot Equations of State", Air Force Weapons Laboratory Report AFWL-TR-69-38, April 1969.

McGlaun, J. M., S. L. Thompson, and M. G. Elrick (1990). "CTH: A Three-Dimensional Shock Wave Physics Code", *Int. J. Impact Engng.*, 10, 351-360.

Metals Handbook (1979). Ninth Edition, Volume 2, Properties and Selection: Nonferrous Alloys and Pure Metals, American Society for Metals.

Mock, W. and W. H. Holt (1983). "Fragmentation Behavior of Armco Iron and HF-1 Steel Explosive-Filled Cylinders", *J. Appl. Phys.*, 54, 2344-2351.

Mott, N. F. (1943). "A Theory of the Fragmentation of Shells and Bombs", British Ministry of Supply Report A. C. 4035.

Picatinny Arsenal (1962a). Drawing 8860620, Projectile, 8 inch, Gas, M426, Picatinny Arsenal Ordnance Corps, Department of the Army, Dover, New Jersey, June 29, 1962.

Picatinny Arsenal (1962b). Drawing 10522519, Projectile, 8 inch, Gas, M426, Picatinny Arsenal Ordnance Corps, Department of the Army, Dover, New Jersey, October 30, 1962.

Silling, S. A. (1994). "Johnson-Cook Fracture Model Implementation in CTH", Sandia National Laboratories Report, 1994.

"Structures to Resist the Effects of Accidental Explosions", TM5-1300/NAV FACP-357-AFM88-32, March 1971.

Teledyne Brown Engineering (1998a). Drawing SB00190, APV AASY / SUPPORT Structure INSTL MMD-2, 2-14-98.

Teledyne Brown Engineering (1998b). Drawing SB00190, View A, APV AASY / SUPPORT Structure INSTL MMD-2, 2-14-98.

APPENDIX A - Summary of Fragmentation Model

In this appendix the equations used in the fragmentation model are summarized for reference purposes. The primary focus in the evaluation of fragment size is the strain rate at the time of fracture. Dynamic fragmentation theories predict an average local fragment size at a given strain rate and temperature, and the number of fragments with this average size is determined by the local mass of the material that fractures. The dynamic fragmentation theories have been described in detail elsewhere (Grady, 1988; Kipp, *et al.*, 1993). Various types of fragmentation mechanisms have been identified, depending on the strain rate and temperature at fracture. The fragmentation theories have been derived assuming spall induced by uniform volumetric dilatation. In practice, fracture can occur in other modes as well, including stretching at low pressure (rings and shells), to accommodate a variety of loading conditions. The data can also be used to determine the mass distribution of fractured material in the solid, liquid, and vapor phases.

These expressions incorporate the essential physical processes of fracture nucleation, growth to failure, and/or quenching as developing fractures communicate their presence to adjacent fracture sites. Fractures continue to nucleate and grow as long as local stretching proceeds. When stretching is fully relieved from both ends of all fragments, no additional fractures can form, and the fragmentation event is complete. These relief waves emanating from completed fractures place limits both on the largest and smallest fragments that can survive the formation and growth process. The number of fragments is constrained by the total energy available to drive the fracture process.

For the present purposes, the average fragment size, S, will be determined in three different fragmentation regimes. These are:

(1) solid spall dominated by fracture toughness, for which

$$S = \left(\frac{\sqrt{24}K_c}{\rho c\dot{\varepsilon}}\right)^{2/3} \qquad (A1)$$

(2) solid spall dominated by the flow stress, for which

$$S = \left(\frac{1.2Y}{\rho\dot{\varepsilon}^2}\right)^{1/2}, \qquad (A2)$$

and (3) liquid spall above the melt temperature, for which

$$S = \left(\frac{48\gamma}{\rho\dot{\varepsilon}^2}\right)^{1/3}. \qquad (A3)$$

In these equations, ρ is the density, $\dot{\varepsilon}$ is the strain rate, c is the sound speed, K_c is the fracture toughness, Y is the yield strength, and γ is the surface tension. The dependence of the fracture toughness, K_c, on temperature, T, is assumed to be

$$K_c = K_{c0}\left(1 - \frac{T - T_{ref}}{T_{melt} - T_{ref}}\right)^{n_K}, \qquad (A4)$$

where K_{c0} is the reference fracture toughness, T_{ref} is the reference temperature, T_{melt} is the melt temperature, and n_k is a constant; the dependence of the yield strength, Y, on temperature and strain rate, $\dot{\varepsilon}$, is assumed to be

$$Y = Y_0\left(1 - \frac{T - T_{ref}}{T_{melt} - T_{ref}}\right)^{n_Y}\left(\frac{\dot{\varepsilon}}{\dot{\varepsilon}_0}\right)^{m_Y}, \qquad (A5)$$

where Y_0 is the reference yield strength, $\dot{\varepsilon}_0$ is a reference value of the strain rate (one per second), and n_y and m_y are constants; and the dependence of the surface energy, γ, on temperature is assumed to be

$$\gamma = \sigma_0\left(1 - \frac{T}{T_C}\right)^{n_\sigma - 1}\left(1 + (n_\sigma - 1)\frac{T}{T_C}\right), \qquad (A6)$$

where σ_0 is the surface tension, T_C is the critical temperature, and n_σ is a constant (Grady, 1996).

The temperature / strain rate transition from brittle to ductile fracture, $\dot{\varepsilon}_{bd}$, is defined by equating the average fragment size in Equation A1 and Equation A2 and solving for the strain rate as a function of temperature,

$$\dot{\varepsilon}_{bd} = \left(\frac{\frac{8}{9}\frac{\rho c^4 (Y_o \varepsilon_c)^3\left(1 - \frac{T - T_{ref}}{T_m - T_{ref}}\right)^{3n_Y - 4n_K}}{K_{c0}^4 \dot{\varepsilon}_0^{3m_Y}}}\right)^{\frac{1}{2-3m_Y}}. \qquad (A7)$$

Similarly, there is a temperature / strain rate transition defining the boundary between ductile and liquid fracture, $\dot{\varepsilon}_{dl}$, determined from Equation A2 and Equation A3,

$$\dot{\varepsilon}_{dl} = \left(\frac{2(Y_0 \varepsilon_c)^3\left(1 - \frac{T - T_{ref}}{T_m - T_{ref}}\right)^{3n_Y}}{9\rho \dot{\varepsilon}_0^{3m_Y} \sigma_0^2\left(1 - \frac{T}{T_C}\right)^{2n_\sigma - 2}\left(1 + (n_\sigma - 1)\frac{T}{T_C}\right)^2}\right)^{\frac{1}{2-3m_Y}}. \qquad (A8)$$

In the present application, the local expansion strain rate in the metal case is determined as a function of time, and monitored with respect to the local strain. When the strain to failure has been exceeded, the strain rate at that time is used in the preceding expressions to determine the dimension of the average fragment.

APPENDIX B - Material Model Parameters

The material parameters used in the exploding munition and fragment impact calculations are summarized in this appendix. The explosive parameters for Composition B (Table B1) are assumed to match those of Comp B Grade A explosive, for which JWL parameters are available (Dobratz and Crawford, 1985).

The equations of state for the inert materials are listed in Table B2. The stainless steel equation of state parameters were obtained from Hixson, et al. (1993). The parameters for the rest of the materials are found in Group GMX-6 (1969). The spall stress for each material has also been included in this table.

The solid materials were all treated with an elastic-perfectly plastic constant yield strength model. These parameters are listed in Table B3. The brass and aluminum properties were extracted from Kohn (1969), the stainless steel properties were obtained from the ASM Metals Progress Databook (1976), the munition case steel properties were estimated from similar carbon steels (~1040-1050) and requirements stated on the drawings (Picatinny Arsenal, 1962b). The ECC steel properties were defined in a SSAB Weldox 500 extra high strength structural plate data sheet.

The fracture property sources were the same as those for the yield strengths. In addition, some use was made of the Johnson-Cook fracture model in CTH (Silling, 1994) to model the failure of the case and APV materials in expansion. This model permits the fracture stress to decay from the initial spall stress to the uniaxial tensile stress at maximum elongation, a practical application to case expansion. The model is used with only pressure dependence,

$$\varepsilon_f = D_2 \cdot \exp(-D_3 P/Y) \qquad (B1)$$

where ε_f is the strain to failure, D_2 and D_3 are constants, P is the pressure, and Y is the yield strength.

The parameters are listed in Table B4. The fragmentation parameters for these materials require the fracture toughness, which is also listed in Table B4.

Table B1: Material Parameters for Comp B Explosive

Parameter	Comp B
Density, ρ (g/cm^3)	1.717
Detonation Velocity (cm/s)	7.980×10^5
C-J Pressure (GPa)	29.5
Ideal Gas Constant, Γ	2.706

Parameter	Comp B
A (dynes/cm^2)	5.242×10^{12}
B (dynes/cm^2)	7.678×10^{10}
C (dynes/cm^2)	1.082×10^{10}
R_1	4.20
R_2	1.10
ω	0.34
C-J Temperature (eV)	0.35

Table B2: Equation of State Parameters for Inert Materials

Parameter	Aluminum (2024)	Steel (Iron)	Neoprene	Water	Brass	Stainless Steel
Density, ρ (g/cm^3)	2.785	7.85	1.439	0.998	8.45	7.96
Sound Speed, C_0 (cm/s)	5.328×10^5	3.574×10^5	2.785×10^5	1.647×10^5	3.726×10^5	4.464×10^5
Linear U_s-u_p Coefficient, S	1.338	1.92	1.419	1.921	1.434	1.544
Gruneisen Constant, Γ_0	2.00	1.69	1.39	0.35	2.04	2.17
Specific Heat, C_v (ergs/g/eV)	1.07×10^{11}	5.18×10^{10}	1.0×10^{10}	4.83×10^{10}	4.49×10^{10}	5.18×10^{10}
Spall Stress (dynes/cm^2)	-15.0×10^9	-39.0×10^9	-1.0×10^9	-1.0×10^9	-14.0×10^9	-39.0×10^9

Table B3: Yield Strength Parameters for Solid Materials

Parameter	Steel (Munition)	Aluminum (2024)	Brass	Stainless Steel 316L	Steel (ECC)
Yield Stress, Y_0 (dynes/cm^2)	6.0×10^9	2.9×10^9	2.0×10^9	2.4×10^9	4.8×10^9
Poisson Ratio, ν	0.279	0.33	0.374	0.283	0.279
Melt Temperature, T_m (eV)	0.156	0.105	0.11	0.143	0.156

Table B4: Fracture Parameters for Solid Materials

Parameter	Steel (Munition)	Stainless Steel 316L	Steel (ECC)
Tensile Stress (dynes/cm^2)	6.8×10^9	5.4×10^9	6.5×10^9
Elongation (%)	15 - 30	55	16
D_2 (J-C Coefficient)	0.163	0.645	0.173
D_3 (J-C Coefficient)	-0.216	-0.200	-0.180
Fracture Toughness K_{c0} (MPa m$^{1/2}$)	100 - 265	250	-

APPENDIX C - Limit Velocity Data / CTH Code Comparison

Two methods to determine the limit velocity for projectile impacts onto thin targets are described in this appendix: CTH code iterative results and an empirical expression, both calibrated to the same experimental data.

In an example with projectile dimensions appropriate to the current fragments and targets, the limit velocity for a steel projectile with L/D=5 impacting a 12.7 mm steel target is 1432 m/s (Grabarek, 1971, from Anderson, et al., 1992). Table C1 lists the details of the experimental conditions.

Table C1: Experimental Data Point for Limit Velocity

Projectile		**Target**	
Length, L (mm)	20.2	Material	RHA
Diameter, D (mm)	4.04	Thickness, t (mm)	12.7
L/D	5.00	Density (g/cm^3)	7.86
M (g)	1.94	BHN	381
Material	Bearcat	Obliquity (deg)	0
Density (g/cm^3)	7.80	**Scaling**	
BHN	560	t/L	0.629
Elong (%)	10.0	t/D	3.144
Results			
V_L (m/s)	1432		

Anderson, et al. (1992) report how the material tensile strength can be related to the Brinell Hardness Numbers, BHN,

$$BHN = 1.979 \cdot [TensileStrength(ksi)] + 11.24 \qquad (C1)$$

On this basis, the projectile tensile strength (BHN 560) is 277 ksi (18.8 kb), and the target tensile strength (BHN 381) is 187 ksi (12.7 kb).

The material parameters used for the two steels in these simulations are listed in Table C2. The Bearcat yield strength was estimated by proportioning it to the yield strength of RHA relative to the two material tensile strengths obtained from the Brinell Hardness Numbers listed in Table C1. The spall stress was used for the fracture stress in both steels.

When this impact geometry is calculated with CTH at the experimental limit velocity (1432 m/s), the projectile exits the target with a residual velocity of 620 m/s. In order to obtain a calculated residual velocity of zero, the impact velocity has to be reduced by 15%, to 1217 m/s.

Figure C1 indicates the initial and final conditions for the impact at 1217 m/s. Although a plug of target has been ejected, the projectile has come to rest, its residue trapped in the target.

Table C2: Summary of steel projectile and target material parameters

Property / Material	Projectile (Bearcat)	Target (RHA)
EOS:		
Density (g/cm^3)	7.85	7.85
Bulk Sound Speed, C_0 (m/s)	3.574×10^5	3.574×10^5
Linear U_s-u_p Constant	1.92	1.92
Gruneisen Coefficient	1.69	1.69
Specific Heat (erg/g/eV)	5.18×10^{10}	5.18×10^{10}
Elastic-Plastic / Fracture:		
Yield Strength ($dynes/cm^2$)	12.0×10^9	7.9×10^9
Poisson Ratio	0.279	0.279
Melt Temperature (eV)	0.156	0.156
Fracture Strength ($dynes/cm^2$)	39.0×10^9	39.0×10^9

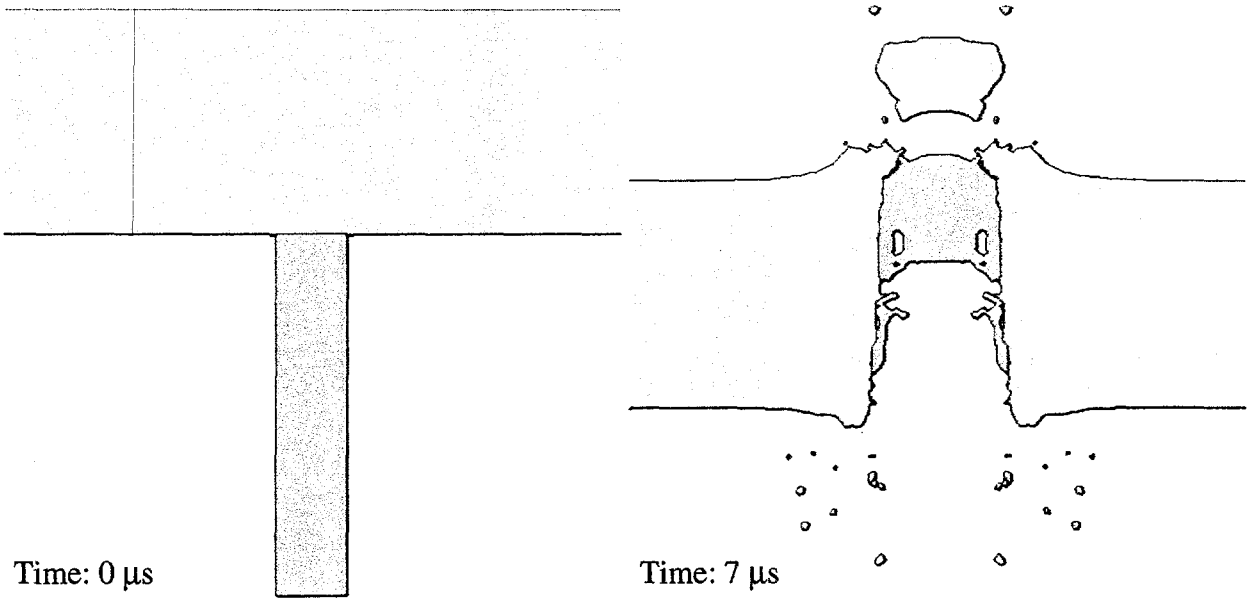

Figure C1. Initial and final conditions for impact at the CTH calculated limit velocity, 1217 m/s, which is 15% less than the experimental data point of 1432 m/s.

The CTH limit velocity simulation results are summarized in Figure C2, where the approach to zero residual velocity is plotted. These CTH calculations were made using a conventional elastic-perfectly plastic model for the deviatoric stresses, and a mixed cell yield model that sets the mixed cell yield to zero when more than one material is present. Fracture was modeled with a maximum principal stress criterion. It was found that when a more detailed treatment of fracture (Johnson-Cook) was employed, the calculated limit velocity was at least 20% less than the experimental data point.

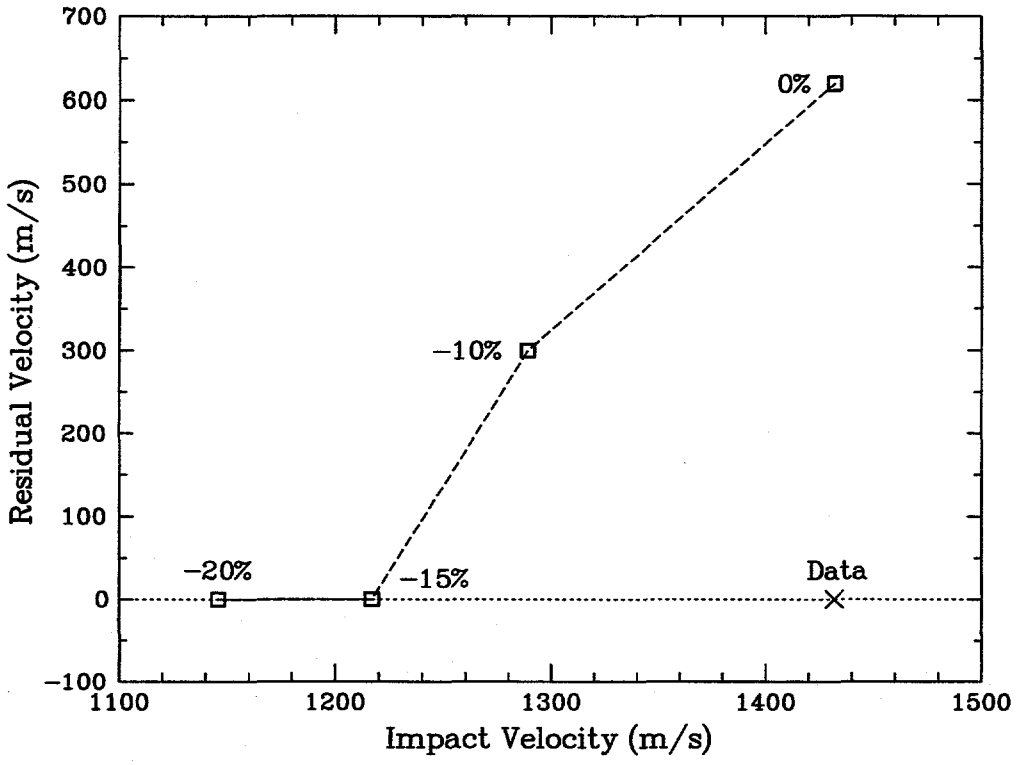

Figure C2. CTH calculated residual velocity as a function of impact velocity. The % labels indicate the offset from the experimental limit velocity.

A variety of penetration formulae have been developed to fit appropriate limit velocity data. For example, the limit velocity for projectile impacts onto finite thickness targets has been described empirically with the expression,

$$V_L^2 = \frac{AD^3}{W}\left(\frac{t \cdot \sec\theta}{D}\right)^{1.6}, \qquad (C2)$$

where V_L is the limit velocity, t is the target thickness, D is the projectile diameter, W is the projectile mass, θ is the projectile incident obliquity (deviation from normal impact), and A is a constant (Gillich, 1975); the units of all quantities are cgs. The relationship can be rewritten in

terms of the projectile length, L, and the projectile density, ρ; for normal impact, Equation C2 takes the form,

$$V_L^2 = \frac{A'}{\rho(L/D)}(t/D)^{1.6}, \qquad (C3)$$

where A' is a constant.

Using the data point from Table C1, the constant A' in Equation C3 is evaluated to be 12.8×10^{10} dynes/cm^2. Three other data points from Anderson, et al. (1992) for steel projectiles and steel targets lead to values for A' of 10.5×10^{10} dynes/cm^2 (L/D=5.0, t/L=0.552, t/D=2.76, V_L=1170 m/s) (Grabarek, 1971, from Anderson, et al., 1992), 11.2×10^{10} dynes/cm^2 (L/D=5.0, t/L=0.392, t/D=1.96, V_L=917 m/s) (Grabarek, 1971, from Anderson, et al., 1992), and 7.8×10^{10} dynes/cm^2 (L/D=1.0, t/L=0.867, t/D=0.867, V_L=890 m/s) (Hohler and Stilp, 1987, from Anderson, et al., 1992), indicating a substantial variation with data sets, steel properties, etc. A choice of 10.0×10^{10} dynes/cm^2 is a reasonable compromise to evaluate the limit velocity for the target of interest (30 mm steel).

APPENDIX D - Observations on Numerical Resolution

Most of the CTH calculations in this report have been made with uniform cell resolution of 1 mm. To determine how observed phenomena, particularly fracture, are affected by resolution, two calculations were made with uniform resolution of 0.5 mm: (1) the full M426 with the APV wall, where the explosive was initiated at the nose, and (2) a munition transverse cross-section, scored for fragment initiation, with the APV wall. Resolution of 0.5 mm provides 19 cells through the thickness of the APV. A comparison of deformation (case and APV fracture) for the full munition is shown in Figure D1. There is little change with resolution for the overall case breakup and APV shape. The radial expansion of both the case and APV are similar, and the thicknesses of the munition case fragments do not appear to be affected by resolution. The explosive product gas confinement that is observed in the 0.5 mm resolution calculation is a numerical effect of no consequence on the motions of interest here. Increased resolution leads to negligible changes in terminal case and APV velocities, as seen in the selected velocity histories compared in Figure D2.

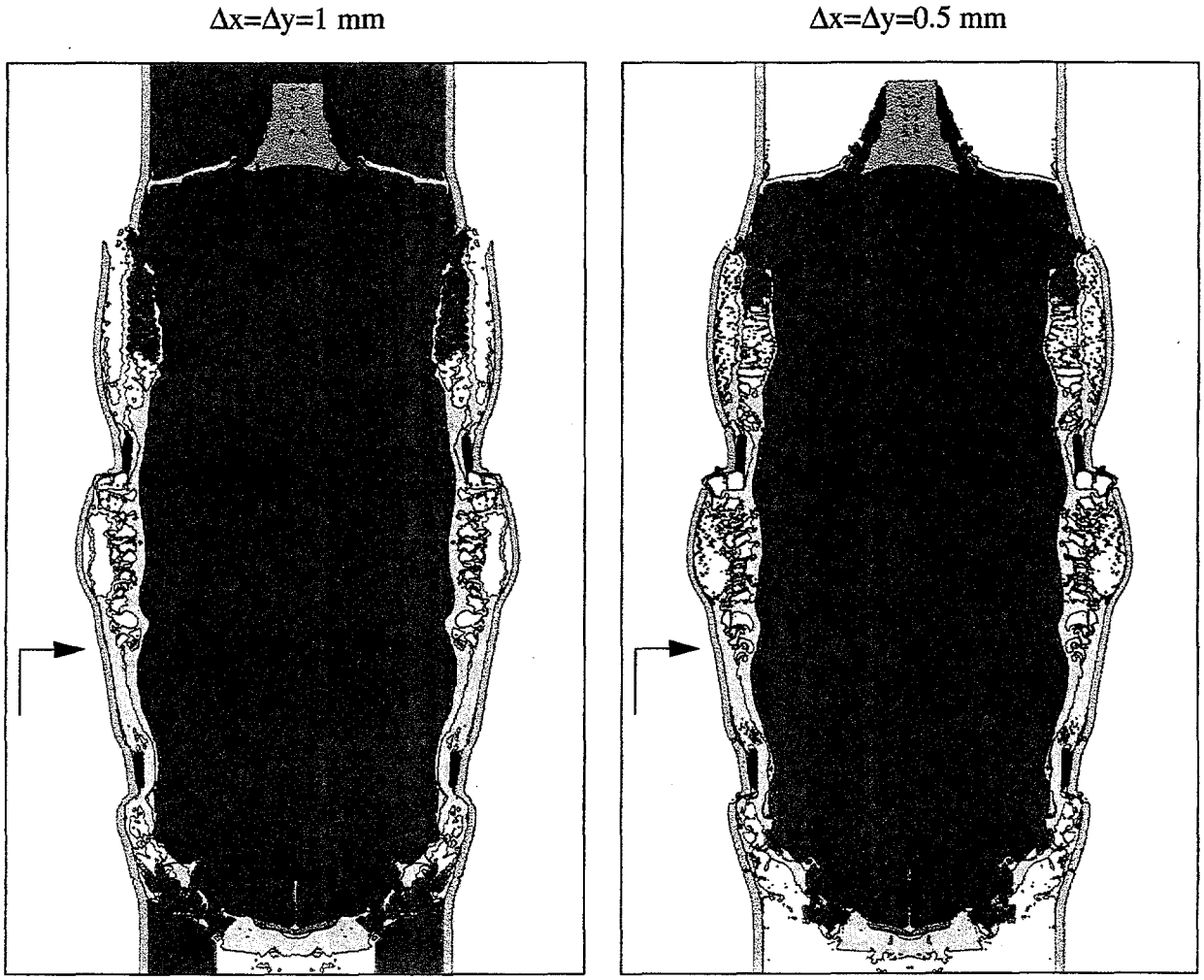

Figure D1. Effect of numerical resolution on CTH calculation of M426 8-inch chemical munition, normal function; 100% agent fill; APV present (Time = 350 μs).

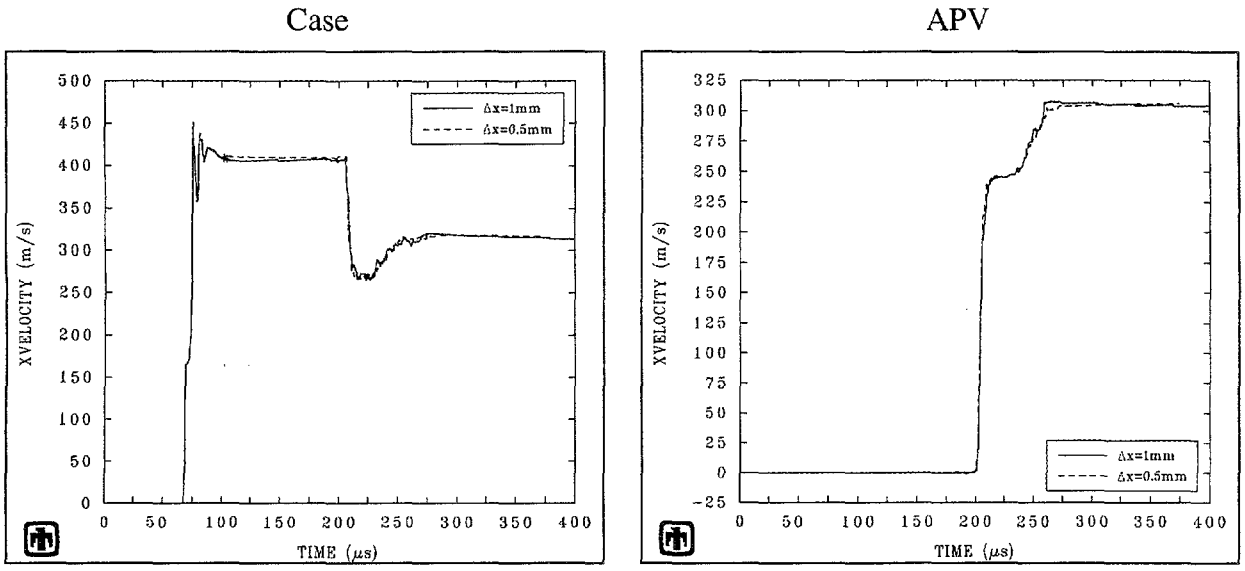

Figure D2. Effect of numerical resolution on case and APV motion (radial expansion velocity) for M426 8-inch chemical munition, normal function; 100% agent fill; APV present. History points are located 25 cm from aft end of munition (arrows in Figure D1).

The 1 mm and 0.5 mm resolution calculations for the transverse munition section with the APV are shown in Figure D3. The munition case was scored in the same locations for both calculations. Here, after the munition case fragments impact the APV, some variations in the final APV fragment lengths and distribution are noticeable. In two locations, sectors that fragmented at 1 mm resolution retained their integrity at 0.5 mm resolution. However, the circumferential dimensions of the final largest fragment remain about 70 mm, independent of resolution. The breakup of the thin explosive burster charge container and shell are also nearly unchanged with resolution. Corresponding velocity histories for munition and APV are plotted in Figure D4 at the location designated by the arrows in Figure D3. This history location is the same as in Figure 13. Both the case and APV display only minor changes in velocity magnitude with improved resolution.

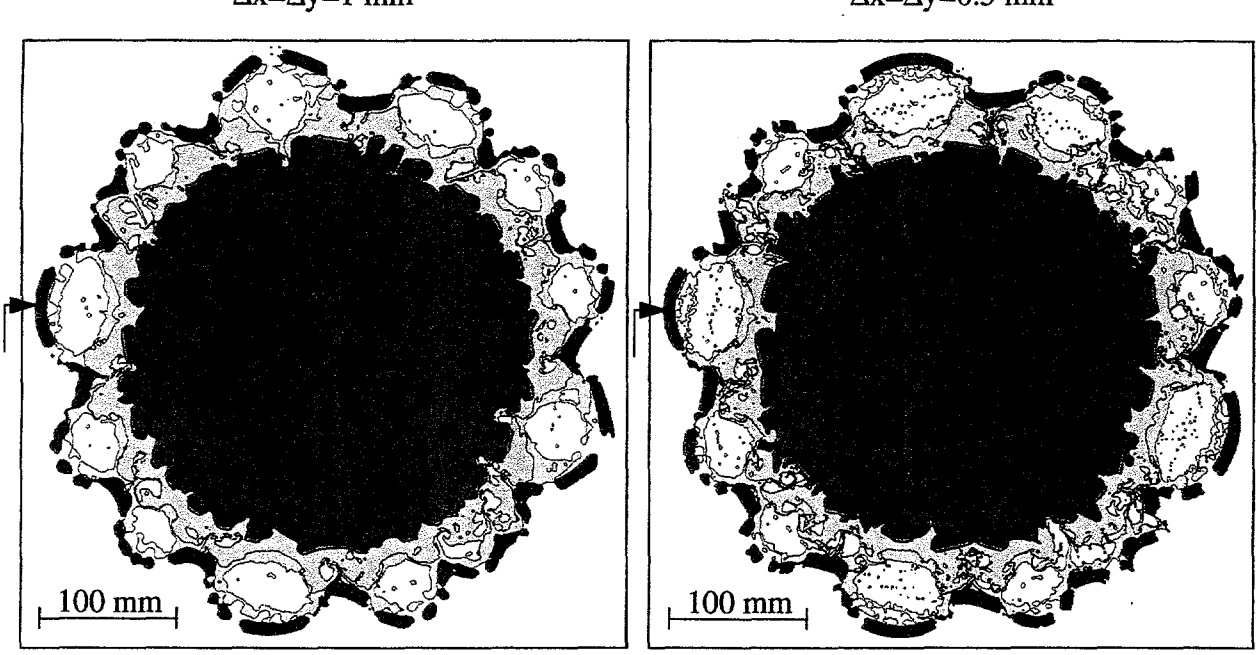

Figure D3. Effect of numerical resolution on CTH calculation of M426 8-inch chemical round transverse section; 100% agent fill, APV present (Time = 250 μs).

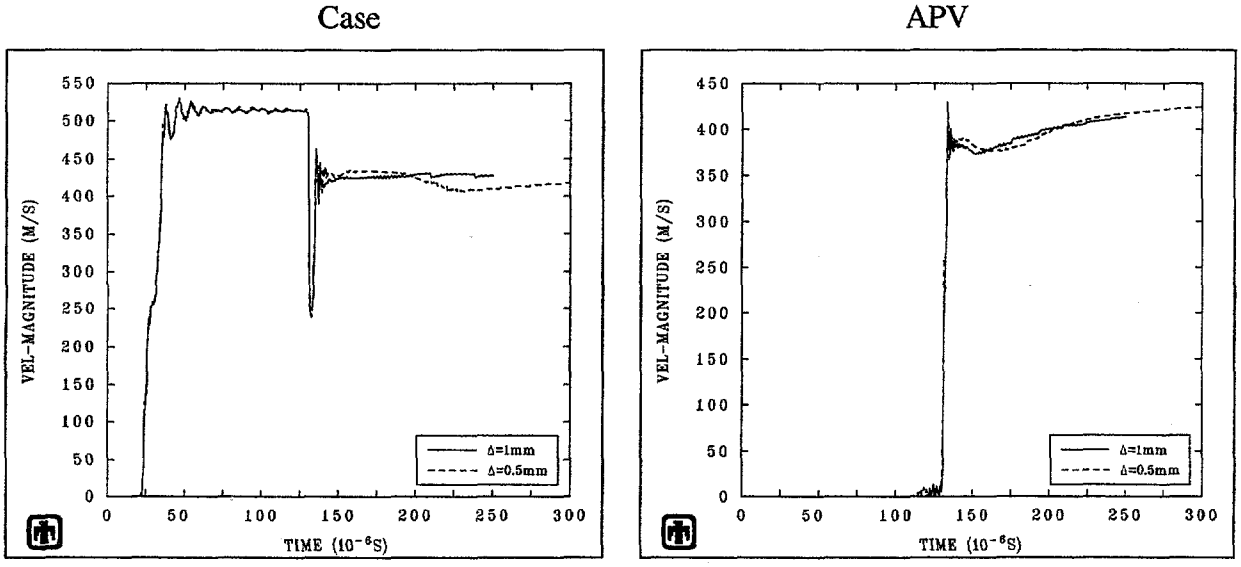

Figure D4. Effect of numerical resolution on case and APV motion for M426 8-inch chemical munition normal function; 100% agent fill; APV present. History points are located in region designated by arrows in Figure D3.

APPENDIX E - Variations of Explosive Initiation Point and Munition Configuration

Initiation points for accidental detonation of the burster charge may not be limited to the fuze-end of the munition, but could occur anywhere along the axis of the charge. Variations in fragment velocity as a function of initiation point are examined in this appendix. In addition, the munition may not be in pristine condition when processed. Estimates of the response to detonation of the burster charge for variations in munition case thickness and presence of agent are obtained here. A few cases are also considered that are intended to provide bounds on fragment characteristics to ensure that the most lethal fragments are used to assess potential damage to the ECC.

A. Center and Fuze-End Initiation of Full Munition

One alternative to fuze-end explosive initiation is an accident scenario that assumes the burster charge is initiated near its center, in response to mechanical activity on the case. That motion is illustrated in Figure E1; complete detonation requires 38 μs. Although there are some overall minor shape differences in the case expansion contour at 200 μs, the response is quite similar to that of normal function (Figure E2). (In each of these configurations, only free case expansion was examined, without the APV present, but with the steel clamps in place.) The fuze-end initiation appears to lead to more expanded agent than is observed in the center-initiated case. The maximum case velocities as a function of axial position for both initiation points are plotted in Figure E3. The largest case velocities are at the fuze end, and are less than 600 m/s. Only minor velocity variations in the munition case are seen for these two initiation points.

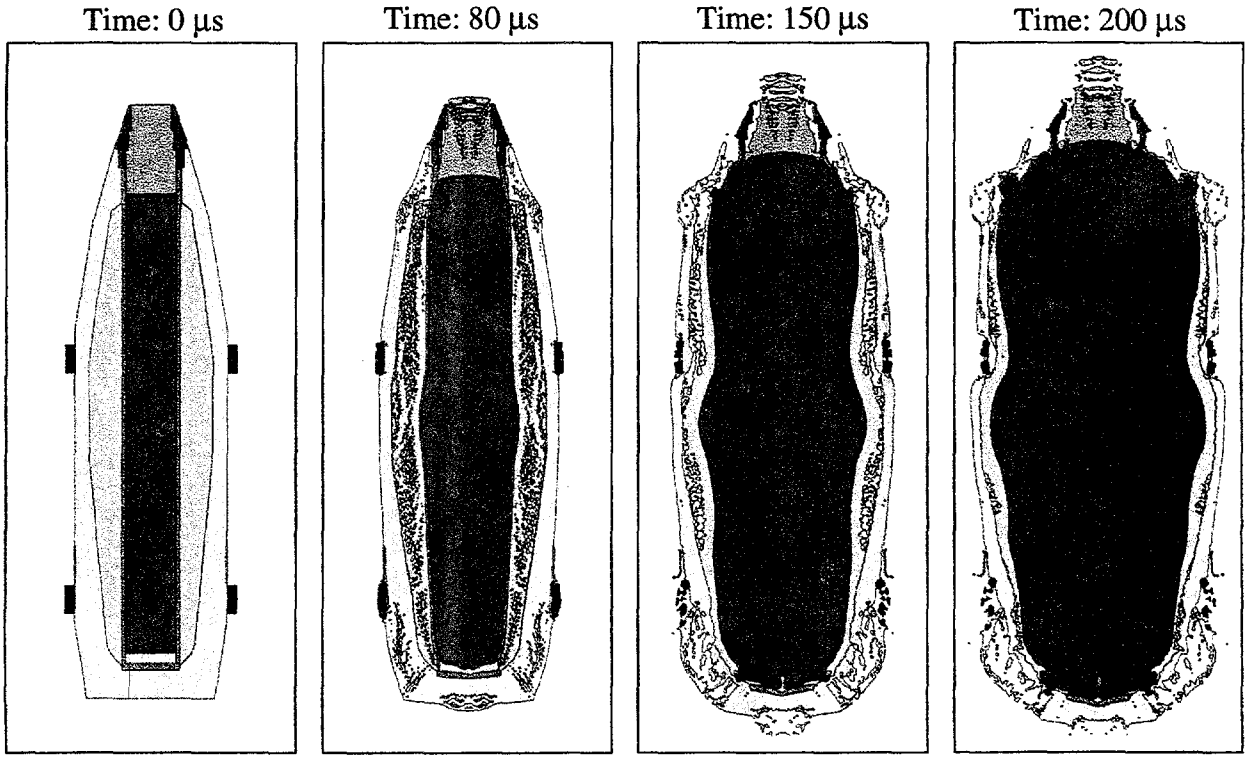

Figure E1. CTH calculation of burster charge function with center initiation for the M426 8-inch chemical round; 100% agent fill.

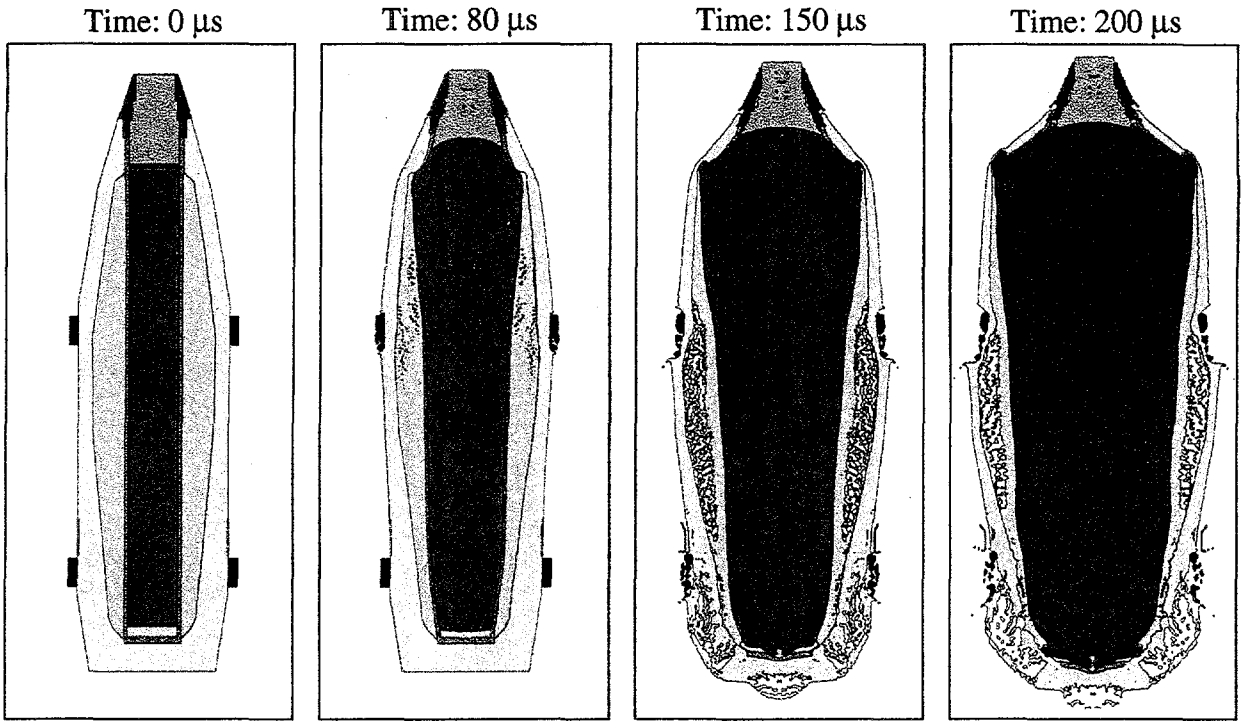

Figure E2. CTH calculation of normal burster charge function (fuze-end initiated) for the M426 8-inch chemical round; 100% agent fill.

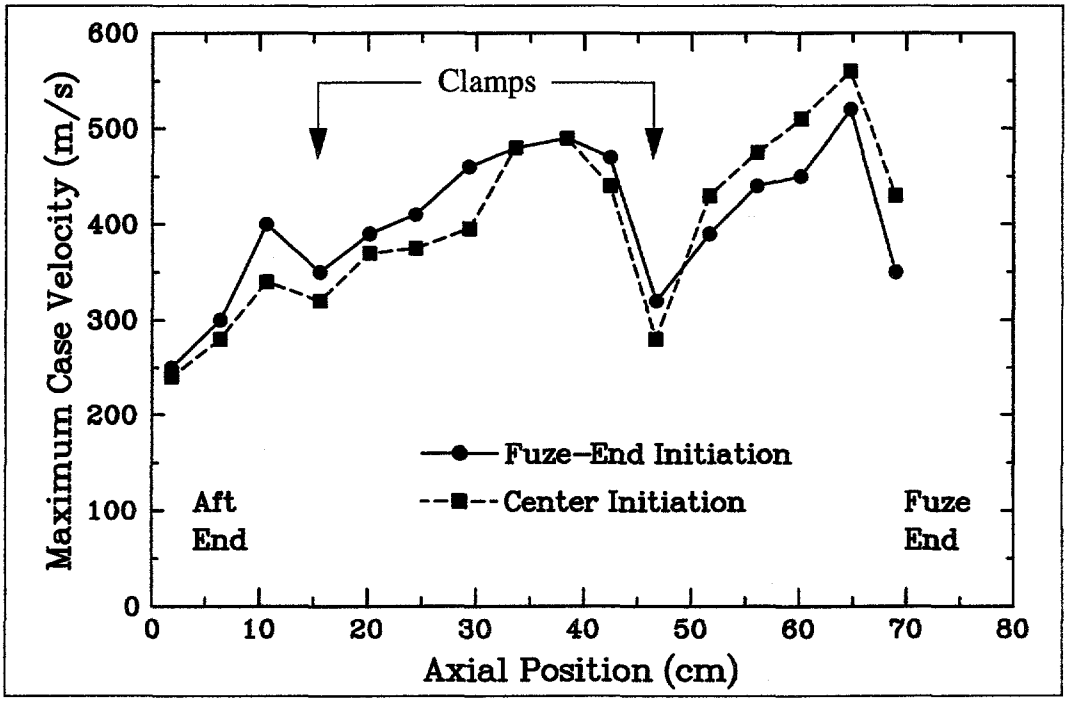

Figure E3. Comparison of maximum munition case velocities for normal (fuze-end) and center initiation of the burster charge in the M426 8-inch chemical round; 100% agent fill.

Four other munition - agent configurations in this axial geometry were calculated: corroded munition case (idealized with one-half pristine thickness) with 100% agent fill; corroded munition with no agent; pristine munition case with no agent (fuze-end initiated and aft-end initiated).

B. Corroded Munition with and without Agent

When the munition case is one-half normal thickness, and agent is present, the shock transmitted through the agent to the munition case from the burster charge accelerates the case as shown in Figure E4. The overall motion is similar to that seen in Figure E2 for the full thickness case. The case fragment velocities are larger than in the pristine munition because the mass ratio of explosive to case is now larger. At a position near the center of the munition (arrow, Figure E4), the case velocity is about 750 m/s, about 50% larger than the velocity at the same location for the pristine munition. The highest velocity occurs near the fuze end, about 800 m/s, which is about 60% larger than for the pristine munition case. At failure, strain rates are now approximately 7000 / s, resulting in estimated average circumferential fragment dimensions of 15 - 30 mm. This dimension is employed later in this appendix to score the cross-section corresponding to this corroded munition (Figure E7).

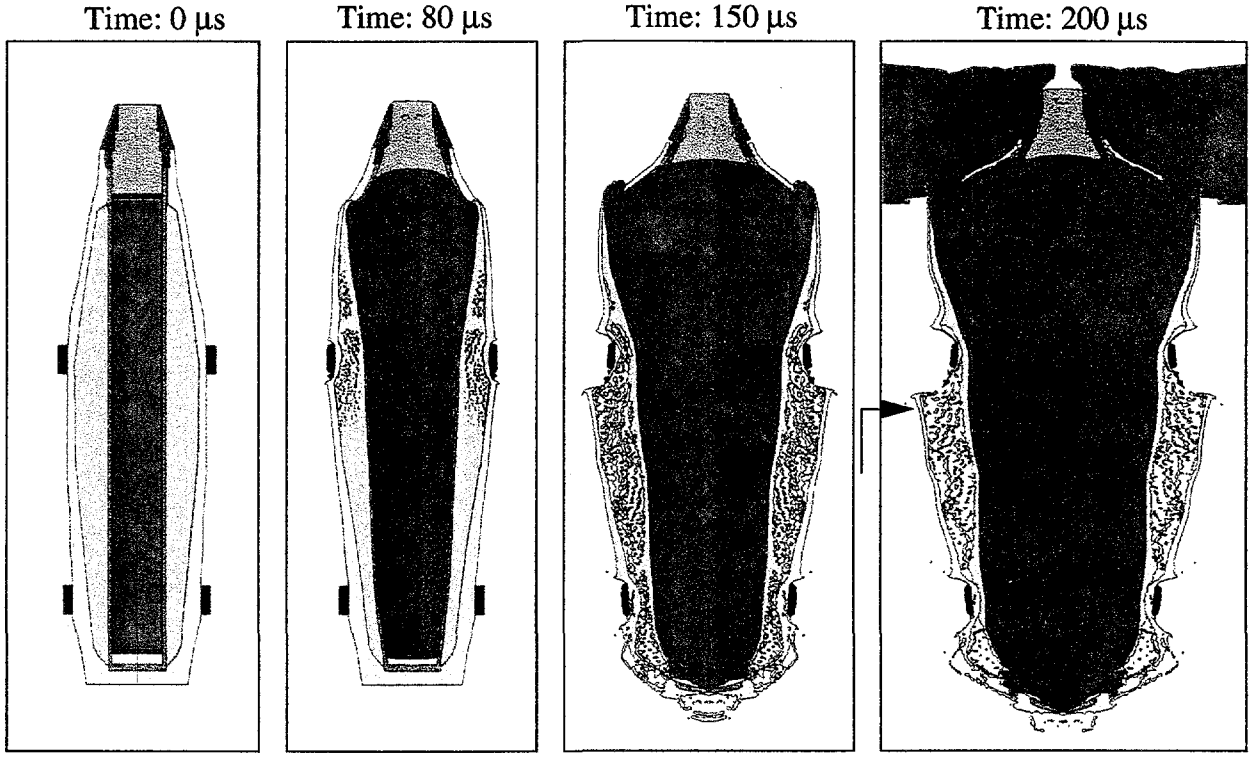

Figure E4. CTH calculation of normal burster charge function (fuze-end initiated) for the M426 8-inch chemical round - 1/2 case wall thickness; 100% agent fill.

When no agent is present for the one-half thickness munition case (Figure E5), the burster case is accelerated directly onto the inside of the munition case at velocities of nearly 1800 m/s. The impact pressure is about 30 GPa. The burster shells are thinner than the munition case, so the internal spall that forms near the outer surface of the case is ejected as a thin layer of the munition, with velocities as large as 1000 m/s. Velocities of the remaining munition case are comparable to those with agent. Figure E6 is a plot comparing the maximum case velocities of these two corroded munitions. Although these terminal case velocities are larger than for the pristine munition, to assess the consequences, interaction with the APV must also be taken into account. Since the case is much thinner compared to pristine conditions, the impact with the APV wall will slow these fragments substantially (discussed in the next section of this appendix).

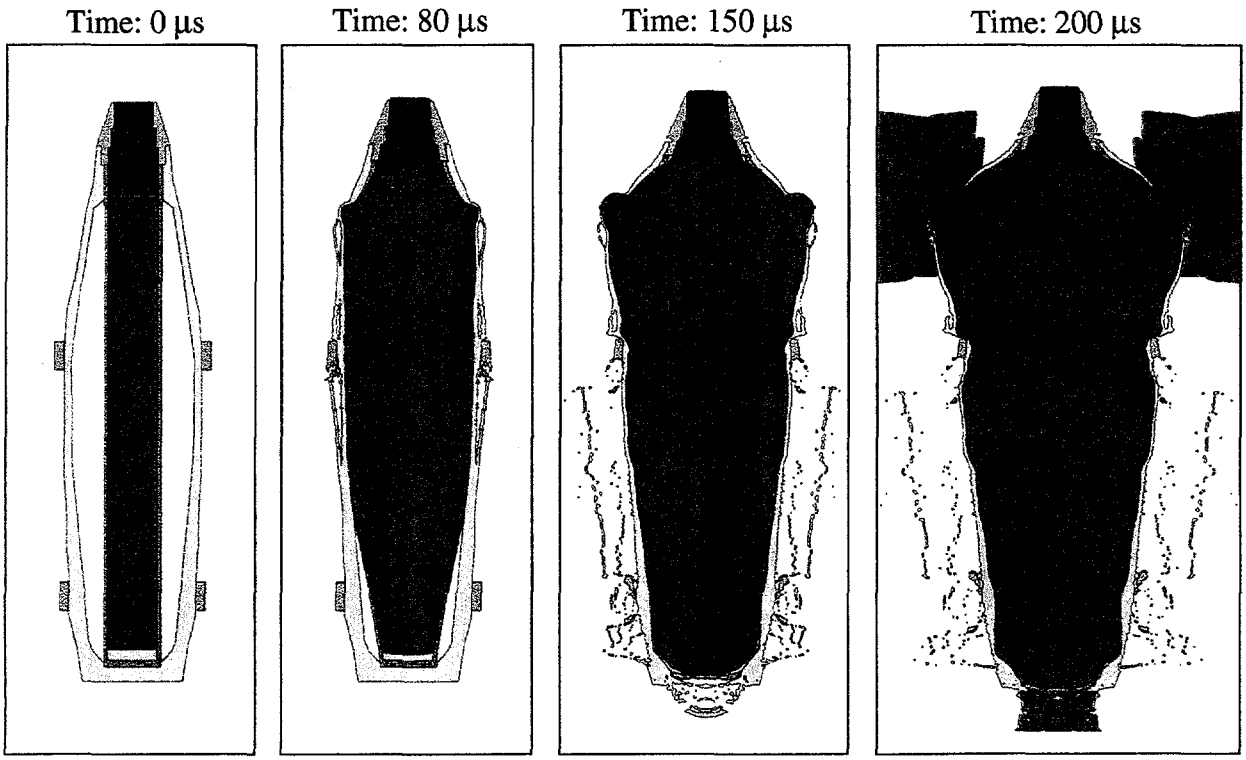

Figure E5. CTH calculation of normal burster charge function (fuze-end initiated) for the M426 8-inch chemical round - 1/2 case wall thickness; without agent.

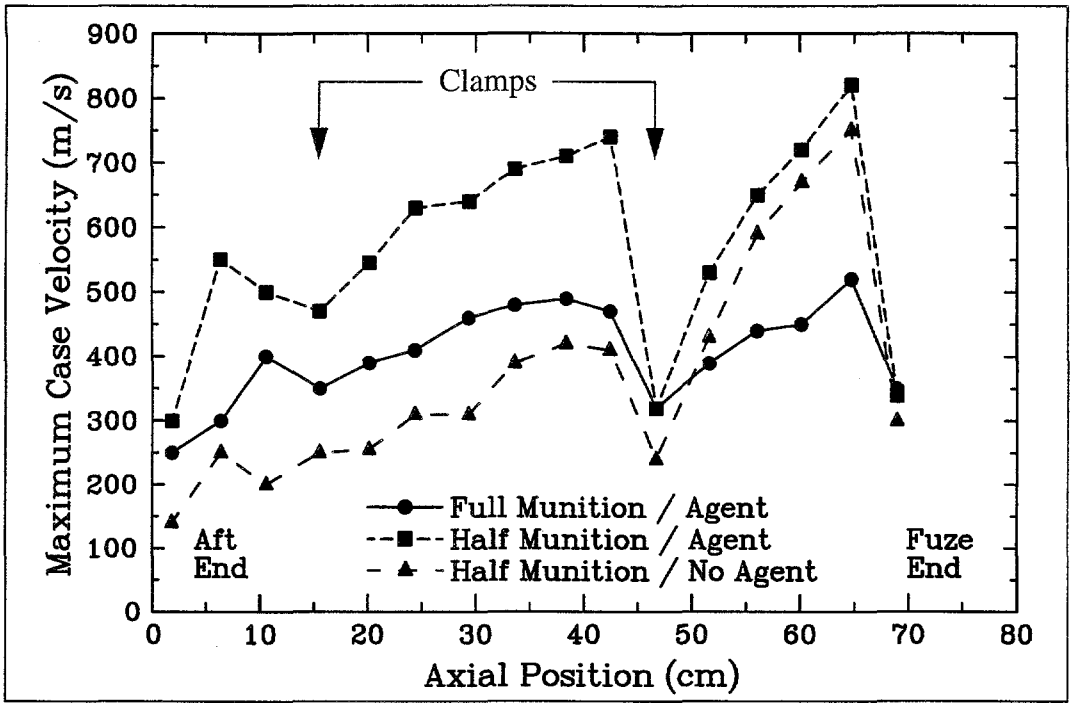

Figure E6. Comparison of maximum munition case velocities for normal (fuze-end) initiation of the burster charge in the M426 8-inch chemical round: 100% agent fill and no agent fill.

C. Corroded Munition Transverse Section with and without Agent

As noted from the results of the one-half thickness munition case, an approximate average fragment size of 25 mm is appropriate for this expansion rate (compared to 45 mm for the pristine munition discussed in the body of the report). When the inside of the munition case is randomly scored for 25 fragments in a transverse section, detonation of the burster charge leads to the sequence of fragment formation and motion recorded in Figure E7.These case fragments are nearly formed by 100 μs, and have broken up the APV by about 150 μs. The impact of the case fragments onto the APV has created a larger number of fragments - both of munition case and APV materials - that in general are smaller than those obtained in the pristine munition (Figure 11), with characteristic maximum dimensions of about 50 mm. Examples of munition-APV interactions are shown in Figure E8, where the impact at about 115 μs slows the munition and accelerates the APV. Acquired APV velocities range from 300 to 400 m/s, depending on location, and impact conditions. Included in these history plots is an example where the impact leads to a final munition fragment velocity that exceeds the APV velocity. Fragments formed from detonation of this corroded munition have the same velocity range as obtained for the pristine munition, but smaller masses. The extent of penetration in the ECC, then, will be less than for the more massive fragments discussed in the main body of this report.

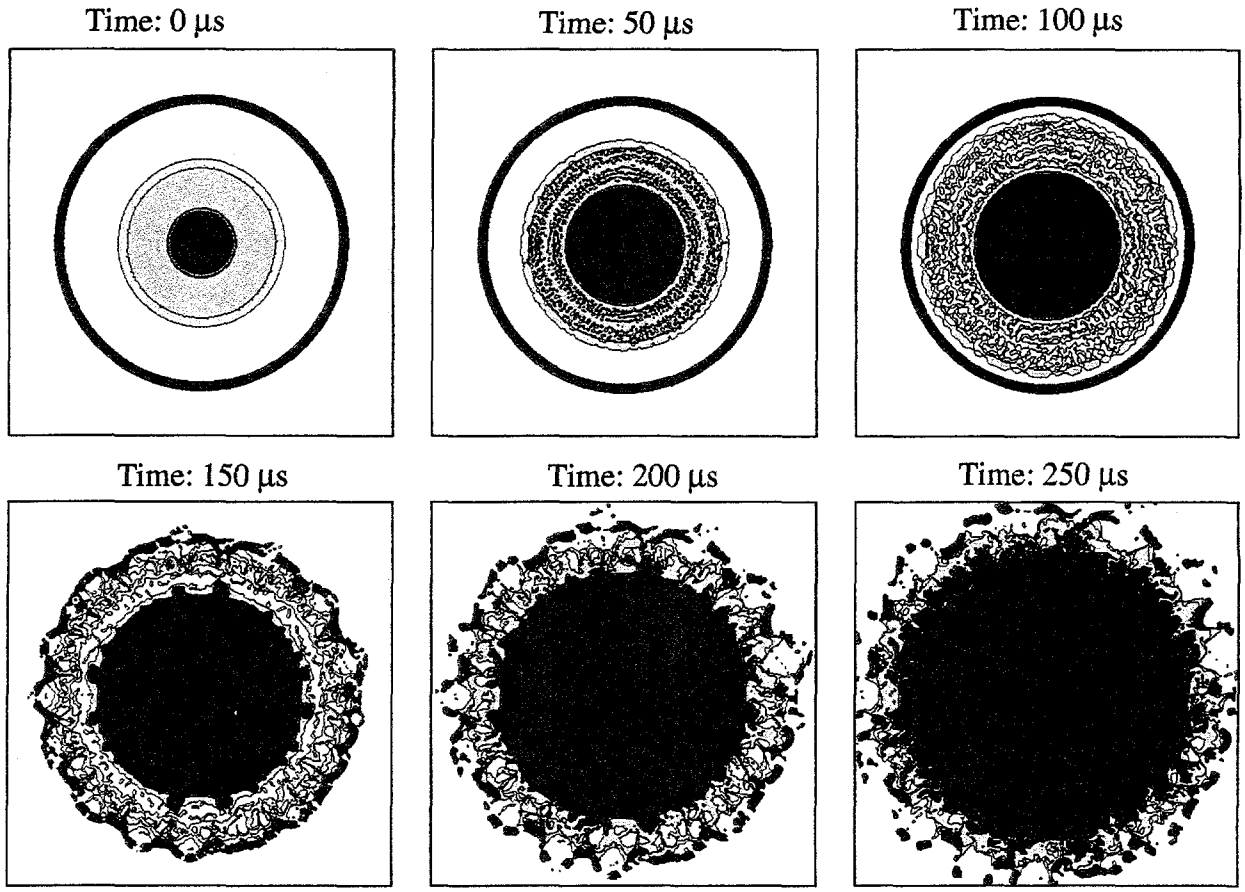

Figure E7. CTH calculation of M426 8-inch chemical round transverse section; 1/2 case thickness; 100% agent fill. Munition case internally scored for 25 fragments.

For the same corroded munition case thickness, when no agent is present (Figure E9), the burster shells are accelerated radially outwards and impact the inside of the munition case. Impact occurs shortly after 35 μs. The impact velocity is about 1700 m/s, shocking the case to about 30 GPa, and spalling a thin layer off the outer surface of the munition case, much in the same way as shown for the full axial munition geometry described in Figure E5. These transverse section velocities and pressure are in good agreement with those from the axial geometry. This spalled layer debris crosses the gap in about 60 μs to impact the APV wall (100 μs), and impart sufficient momentum to cause the APV to accelerate outwards and begin to break up (150 μs). The remaining munition case also breaks up by about 150 μs (in this calculation, the case was not scored), allowing the explosive product gas to escape. Examples of munition and APV fragment velocities at three locations are plotted in Figure E10, and indicate that the spalled layer accelerates the APV fragments to velocities of about 200 m/s. The munition case velocities (about 400 m/s) are larger than the APV velocities, so the munition fragments will eventually overtake the APV fragments. The largest characteristic APV fragment dimensions are now about 60 mm, larger than when agent is present, a consequence of the smaller strain rates during the case fracture. As in the previous

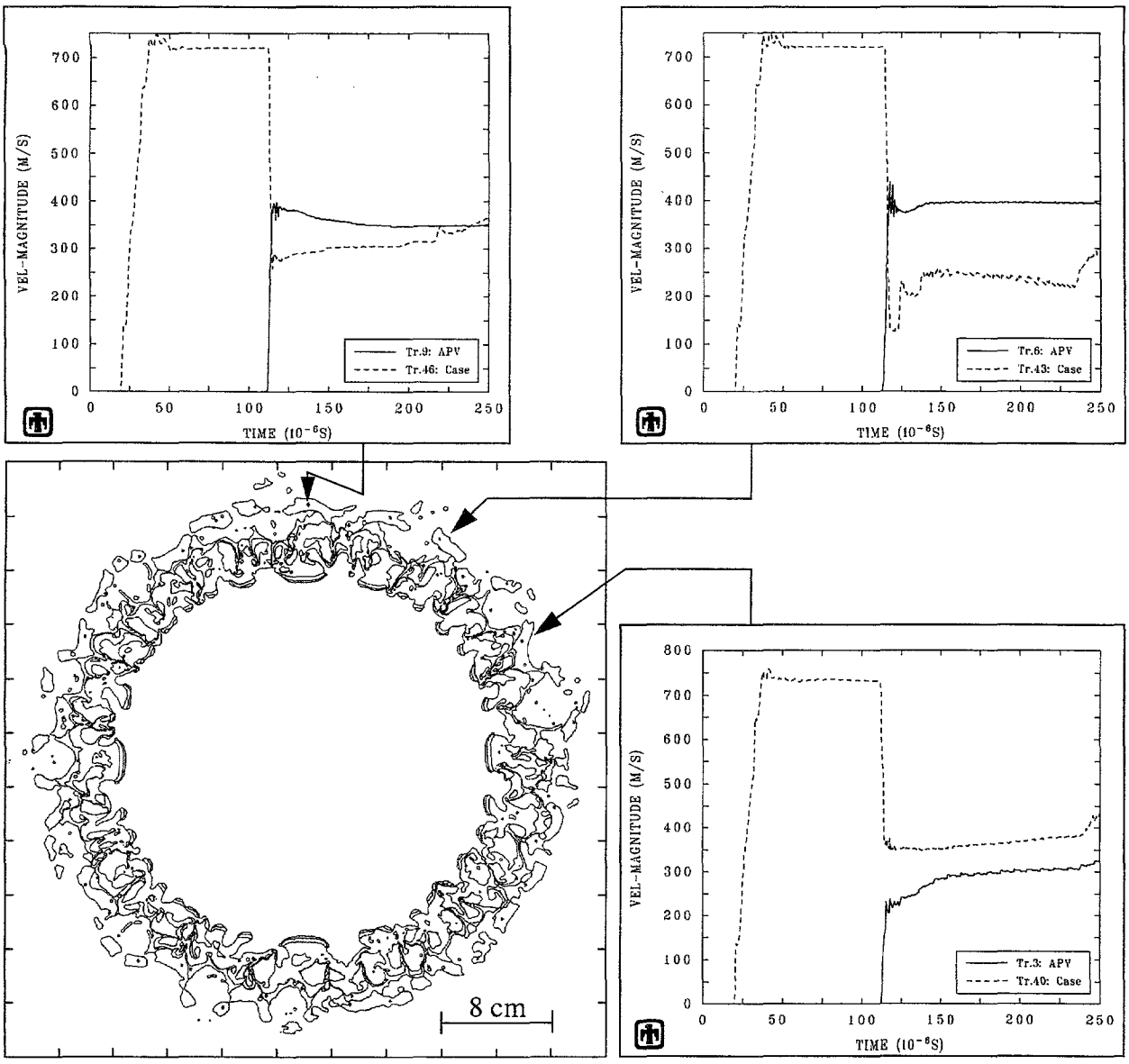

Figure E8. Comparison of munition case and APV velocities at three locations; 1/2 case thickness; 100% agent fill. Internally scored munition case

transverse section, these fragment characteristics are also within the bounds of velocities and dimensions of the fragments discussed in the main body of the report, and not expected to pose any more damaging conditions to the ECC.

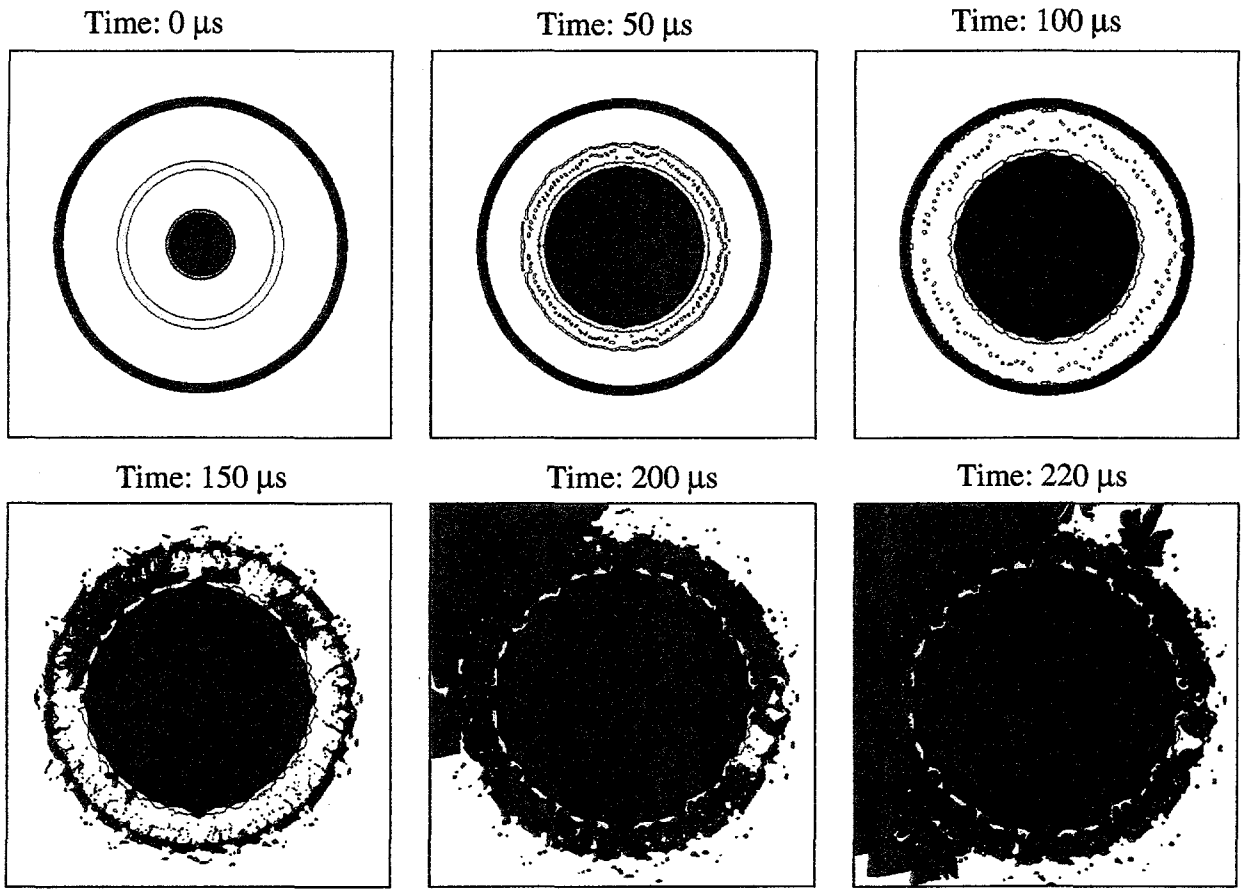

Figure E9. CTH calculation of M426 8-inch chemical round transverse section; 1/2 case thickness; without agent.

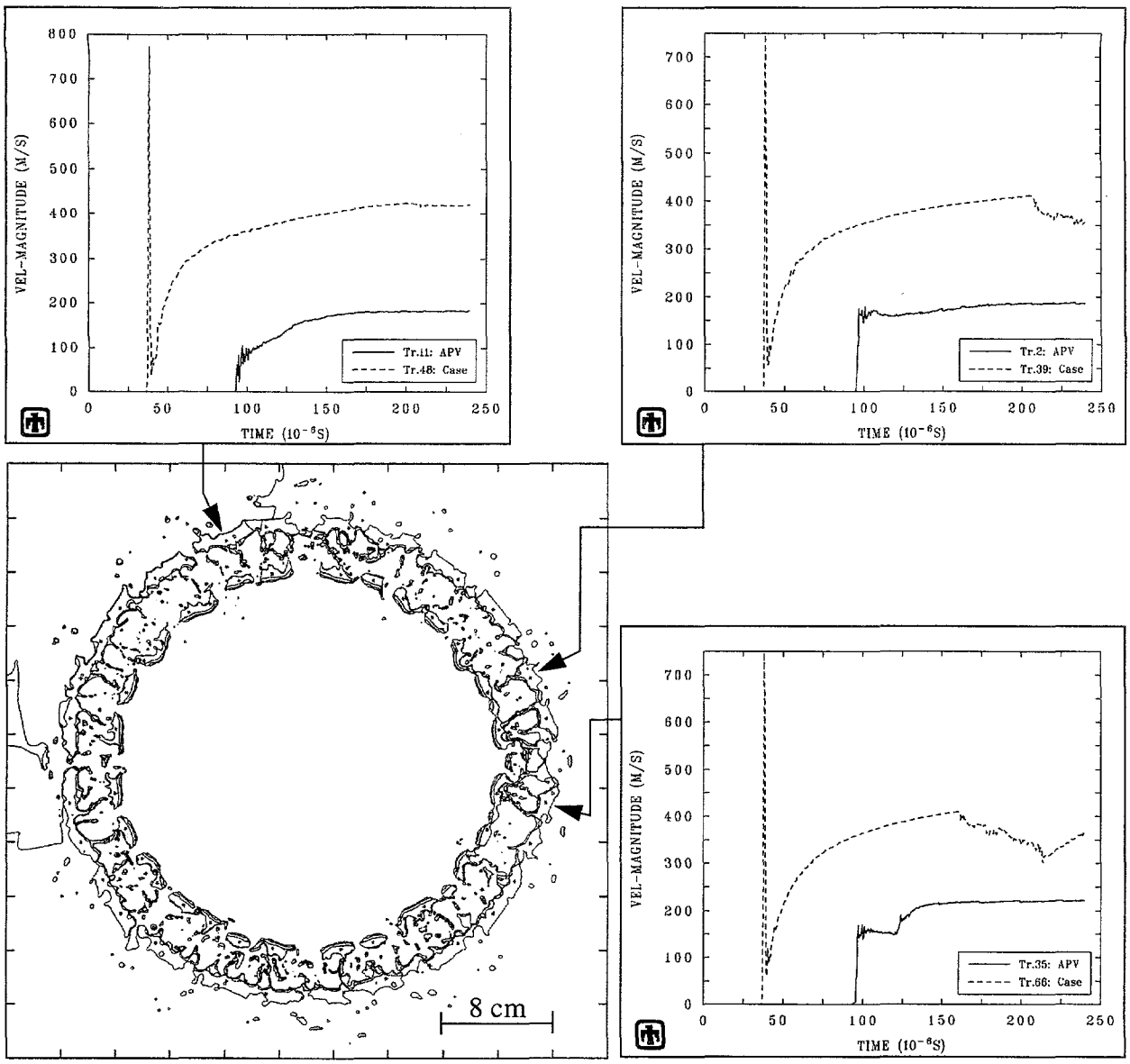

Figure E10. Comparison of munition case and APV velocities at three locations; 1/2 case thickness; without agent.

D. Pristine Munition without Agent: Fuze-End and Aft Initiation

One other configuration of the full munition was analyzed: a pristine munition case, with no agent present. The effects of the burster charge initiated at the fuze end (Figure E11) were compared with initiation at the aft end (Figure E12). (No clamps were present in this configuration.) As observed earlier, when the agent is absent, the burster charge aluminum case and inner steel shell expand at velocities of about 1.6 km/s, impacting the munition case with pressures of 30 GPa. After the thin pulse reflects from the outer free case surface, internal tensions form, spall occurs, and thin shells of munition steel are ejected. The spalled layer is ejected from the exterior of the munition case over nearly the entire length of the munition for fuze-end initiation, and over the full length of the munition case for aft-end initiation. Velocities of this spalled layer range from 400 m/s to about 1000 m/s; the largest velocities occur for the aft-initiated scenario. One-dimensional calculations of this geometry indicate that the outermost spalled layer thickness is about 1.5 mm, with a strain rate at failure (15% strain) of 9000 /s, which corresponds to average circumferential fragment dimensions of 13 - 25 mm, depending on material properties. A fragment characterized by dimensions of 1.5 x 20 x 80 mm (L/D=4) would have a mass of about 20 g. Given a striking velocity of 1000 m/s, this fragment exceeds the calculated (CTH) limit velocity curve in Figure 22, and is at the limit velocity for the empirical curve. Two-dimensional calculations show that an equivalent rod 6 mm diameter by 80 mm length will perforate the 30 mm inner plate of the ECC and penetrate the outer 15 mm layer to a depth of about 5 mm. A three-dimensional simulation of a 1.5 x 20 x 80 mm fragment impacting at 1000 m/s is shown in Figure E13. The fragment perforates the inner 30 mm inner plate of the ECC and causes a bulge in the outer 15 mm layer, but does not have sufficient residual material to penetrate the outer layer.

The velocity of the main case ranges from 150 m/s (aft) to 450 m/s (forward), as observed in the plots of maximum velocity in Figure E14. Again, the influence of initiation point on maximum velocity is not large, and does not alter the peak by more than 20%. At all positions, the maximum case velocities without agent are less than those for a munition with agent (the curve with agent is from Figure 7, where clamps were included in the analysis, causing the local dips in the maximum velocity). In these free expansion scenarios, the circumferential strain rate is about 4500 /s at the location of largest velocity (450 m/s) for fuze-end initiation (axial position of 65 cm, Figure E14). The corresponding characteristic circumferential dimensions of these fragments at the forward end of the munition are approximately 20 - 40 mm. The munition case thickness at the time of fracture (60 μs) is about 20 mm. In the axial direction, 15% strain is exceeded by 100 μs, with a strain rate of about 2000 /s. The fragment lengths range from 35 to 70 mm in this direction. Forming a rectangular fragment from the largest of these dimensions (40 x 20 x 70 mm) leads to a mass of about 450 g. A fragment of this mass and velocity falls below the limit velocity curve shown in Figure 22 for the ECC inner wall. At all other axial locations, the velocities are within the bounds previously determined to be insufficient to perforate the inner ECC wall.

Consequently, without the APV to moderate the fragment velocities, the integrity of the ECC does not appear to be compromised by the larger, slower residual fragments from the drained munition, but the small, high-velocity fragments formed by the spall layer are quite capable of perforating the inner wall of the ECC.

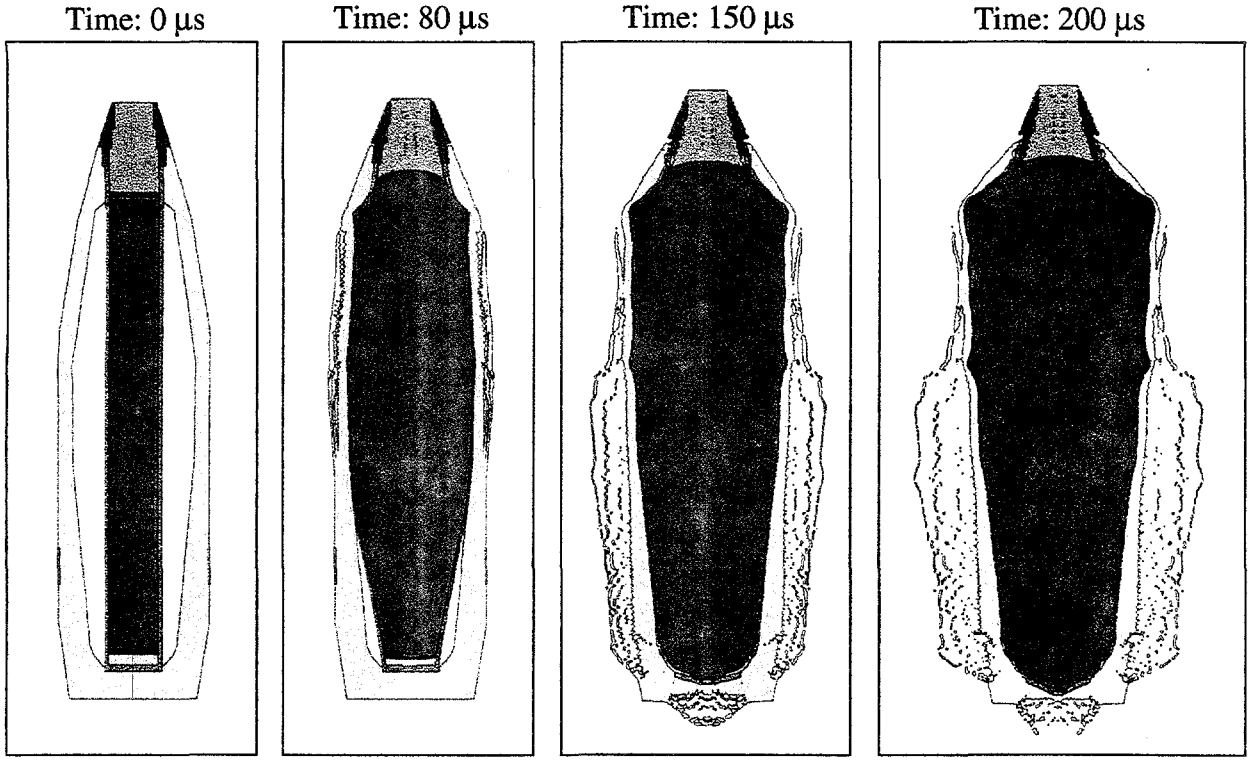

Figure E11. CTH calculation of normal burster charge function (fuze-end initiated) for the M426 8-inch chemical round - normal case wall thickness; without agent.

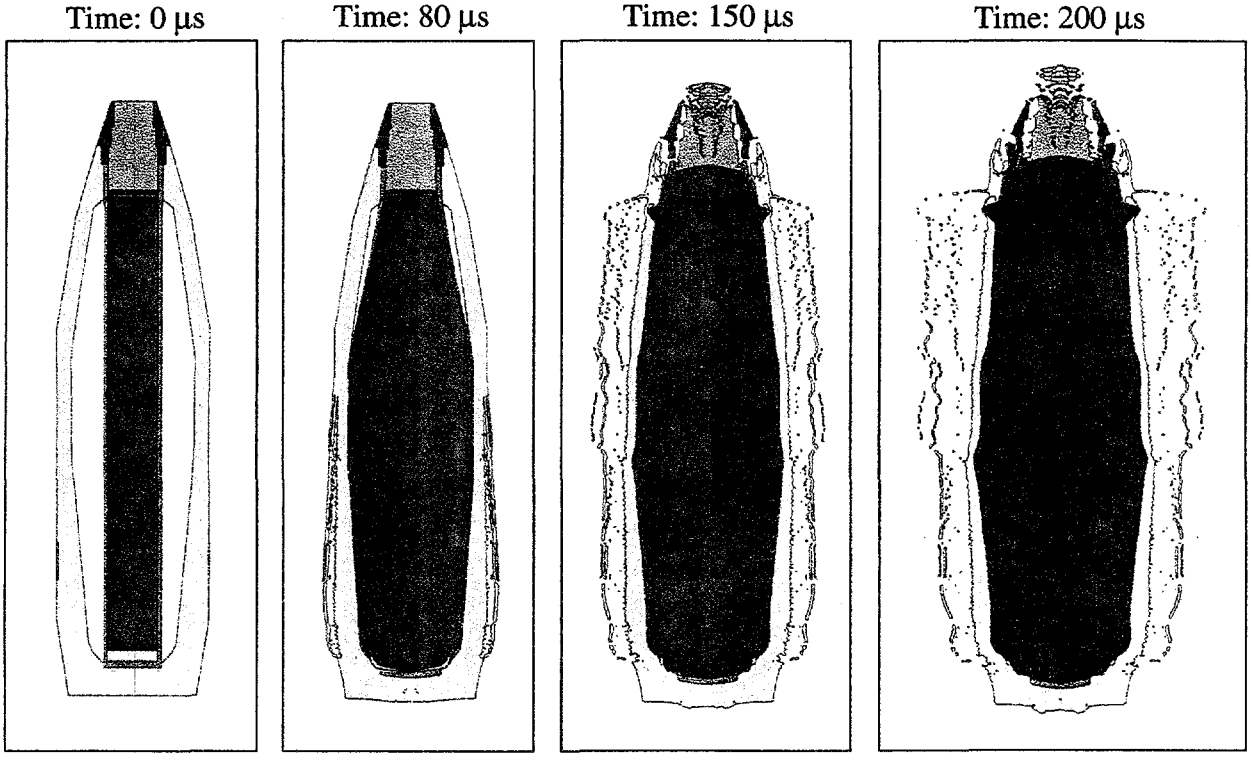

Figure E12. CTH calculation of burster charge function (aft-end initiated) for the M426 8-inch chemical round - normal case wall thickness; without agent.

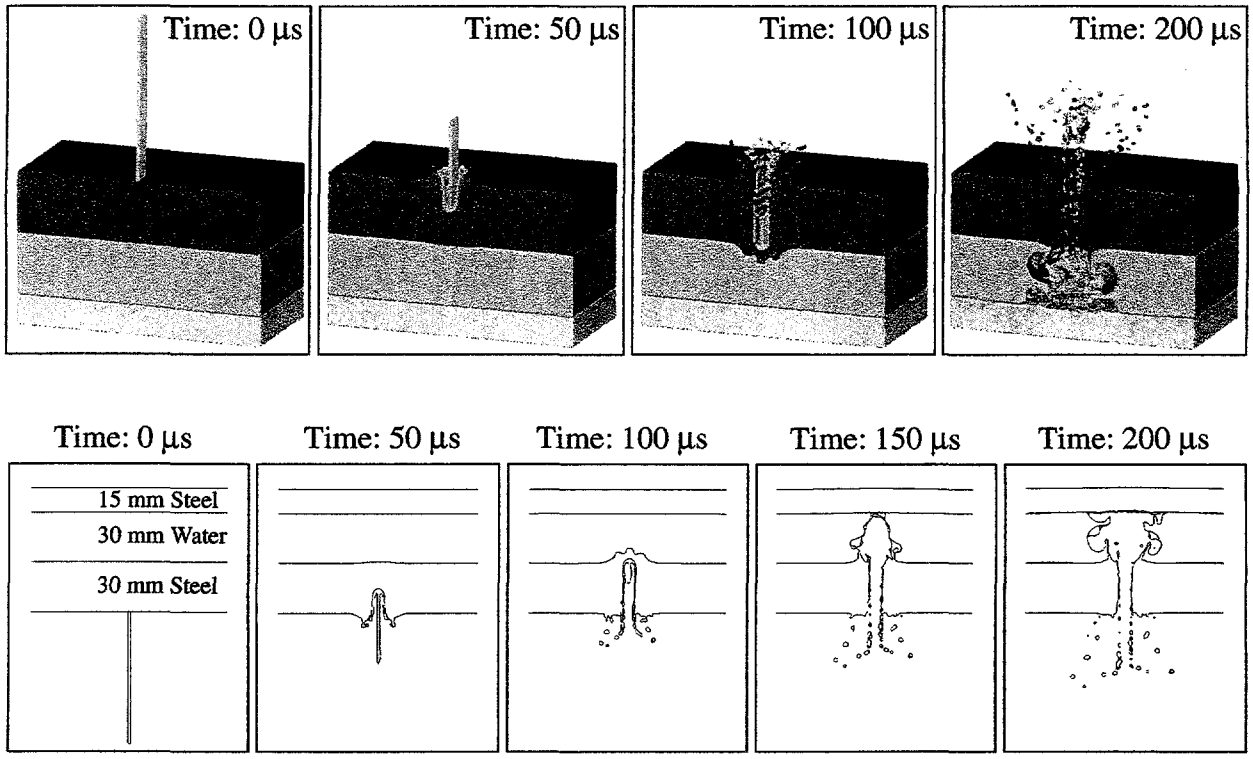

Figure E13. Fragment 4 (20 g, 1000 m/s) normal impact onto the ECC. Upper row, three dimensional views; lower row, cross-section view in the symmetry plane.

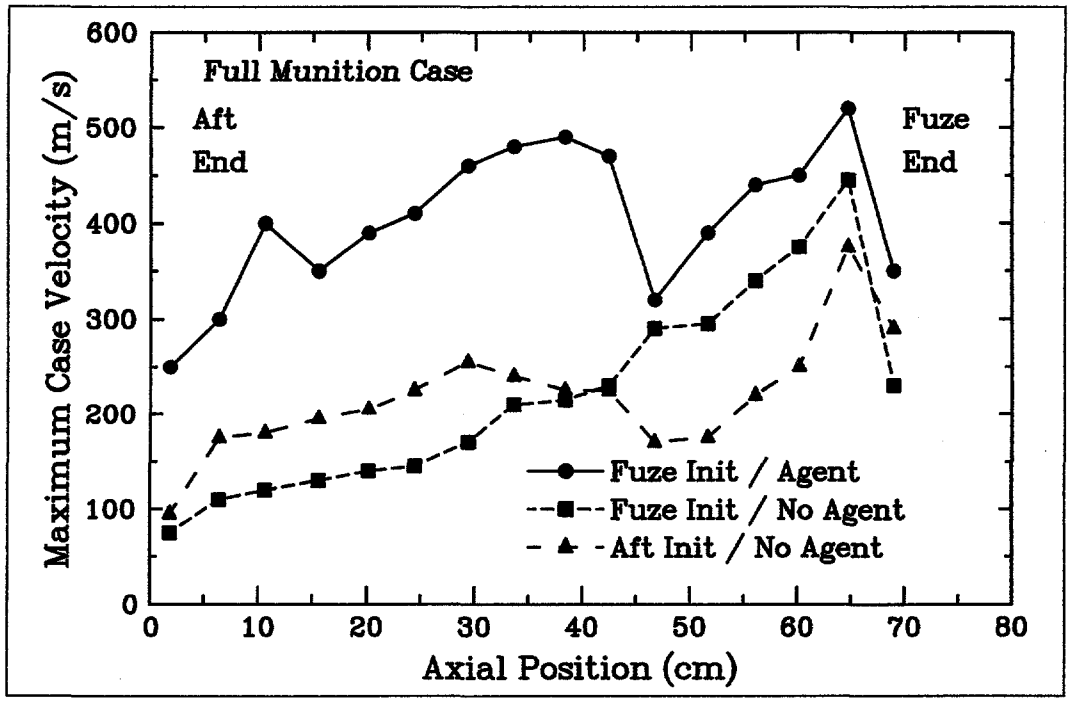

Figure E14. Comparison of maximum munition case velocities for normal (fuze-end) and aft initiation of the burster charge in the M426 8-inch chemical round; no agent fill.

(This Page Intentionally Left Blank)

DISTRIBUTION

INTERNAL

MS 0619 Review and Approval Desk, 15102, For DOE/OSTI (2)
MS 0899 Technical Library, 4916 (2)
MS 9018 Central Technical Files, 8940-2

MS 0321 W. J. Camp, 9200
MS 0437 J. W. Swegle, 9117
MS 0437 R. K. Thomas, 9104
MS 0443 H. S. Morgan, 9117
MS 0819 D. E. Carroll, 9231
MS 0819 E. S. Hertel, 9231
MS 0819 J. S. Peery, 9231
MS 0820 P. Yarrington, 9232
MS 0820 M. E. Kipp, 9232 (10)
MS 0820 R. R. Martinez, 9232 (5)
MS 0820 S. A. Silling, 9232
MS 0820 P. A. Taylor, 9232
MS 0834 A. C. Ratzel, 9112
MS 0834 M. R. Baer, 9112
MS 1156 P. W. Cooper, 9322
MS 1452 J. A. Merson, 1552
MS 1453 R. A. Benham, 1553 (5)
MS 1453 F. H. Braaten, Jr., 1553
MS 1453 T. L. Garcia, 1553
MS 1453 M. C. Grubelich, 1553
MS 1453 W. G. Rivera, 1553
MS 1454 S. H. Fischer, 1553 (5)
MS 1454 L. L. Bonzon, 1554
MS 9004 M. E. John, 8100
MS 9042 E. P. Chen, 8742
MS 9042 M. L. Chiesa, 8743
MS 9042 J. J. Dike, 8743
MS 9105 H. H. Hirano, 8119
MS 9105 B. L. Haroldsen, 8118
MS 9105 J. A. Lamph, 8118
MS 9105 A. McDonald, 8118
MS 9105 K. L. Tschritter, 8119 (5)
MS 9409 W. C. Replogle, 8270

EXTERNAL

Col. Edmund Libby
Project Manager for Non-Stockpile Chemical Materiel
ATTN: SFAE-CD-N, Bldg E4405
APG, MD 21010-5401

Donald Benton
Non-Stockpile Chemical Materiel Program
ATTN: SFAE-CD-NP
Bldg E4410
APG, MD 21010-5401

Alan Caplan
Non-Stockpile Chemical Materiel Program
ATTN: SFAE-CD-NP
Bldg E4410
APG, MD 21010-5401

Ray DiBerardo
Non-Stockpile Chemical Materiel Program
ATTN: SFAE-CD-NP
Bldg E4410
APG, MD 21010-5401

Michael L. Duggan
Project Manager
ATTN: AMCPM-NSP
Bldg E4405
APG, MD 21010-5401

Larry Gottschalk
Non-Stockpile Chemical Materiel Program
ATTN: SFAE-CD-NP
Bldg. E4410
APG, MD 21010-5401

Jerry Hawks (6)
Non-Stockpile Chemical Materiel Program
ATTN: SFAE-CD-NP
Bldg E4410
APG, MD 21010-5401

Charles L. Heyman
Chief, Project Management Office
Non-Stockpile Chemical Materiel Program
ATTN: SFAE-CD-NM
Bldg. E4405
APG, MD 21010-5401

Wayne Jennings
Deputy Program Manager for Non-Stockpile
Chemical Materiel
ATTN: SFAE-CD-NP
APG, MD 21010-5401

K. Kimsey
AMSRL WM TC
U. S. Army Research Laboratory
Aberdeen Proving Ground, MD 21005-5066

M. Lampson
AMSRL WM TC
U. S. Army Research Laboratory
Aberdeen Proving Ground, MD 21005-5066

M. N. Raftenberg
AMSRL WM TD
U. S. Army Research Laboratory
Aberdeen Proving Ground, MD 21005-5066

W. Emerson Rudacille, Jr.
Project Engineer
Non-Stockpile Chemical Materiel Program
Post Office Box 216
APG, MD 21010-0216

Warren Taylor
Non-Stockpile Chemical Materiel Program
ATTN: SFAE-CD-NP
Bldg E4410
APG, MD 21010-5401

David Childers
Project Manager
Non-Stockpile Chemical Demilitarization
Teledyne Brown
Cummings Research Park
P.O. Box 070007
Huntsville, AL 35807-7007

Keith Johnson
Teledyne Brown
Chemical System Analyst
Non-Stockpile Chemical Demilitarization
Cummings Research Park
P.O. Box 070007
Huntsville, AL 35807-7007

Ron A. Marino
Project Manager
Non-Stockpile Chemical Demilitarization
Teledyne Brown
Cummings Research Park
P.O. Box 070007
Huntsville, AL 35807-7007

Larry Maupin
Program Manager
Non-Stockpile Chemical Demilitarization
Teledyne Brown
Cummings Research Park
P.O. Box 070007
Huntsville, AL 35807-7007